Endocrine therapy synergizes with SMAC mimetics to potentiate antigen presentation and tumor regression in hormone receptor-positive breast cancer

Authors:

Francisco Hermida-Prado[1,2,3], Yingtian Xie[1,2], Shira Sherman[1,2], Zsuzsanna Nagy[1,2], Douglas Russo[1,2,4] Tara Akhshi[1,2], Zhengtao Chu[5] , Avery Feit[1,2], Marco Campisi[2], Minyue Chen[2,6], Agostina Nardone[1,2], Cristina Guarducci[1,2], Klothilda Lim[1], Alba Font-Tello[1], Irene Lee[1,2], Juana García-Pedrero[3], Israel Cañadas[7], Judith Agudo[8,9], Ying Huang[10], Tal Sella[2,8,11], Qingchun Jin[4], Nabihah Tayob[4,8], Elizabeth A Mittendorf[8,11,12], Sara M Tolaney[2,8,11], Xintao Qiu[1], Henry Long[1], William F. Symmans[13], Jia-Ren Lin[14], Sandro Santagata[14,15], Isabelle Bedrosian[16], Denise A. Yardley[17,18], Ingrid A Mayer[19], Edward T Richardson[8,15], Giacomo Oliveira[2,8], Catherine J. Wu[8,20,21], Eugene F. Schuster[22,23], Mitch Dowsett[22,23], Alana L. Welm[5], David Barbie[2,8], Otto Metzger[2,8,11#], Rinath Jeselsohn[1,2,8,11#]

Affiliations:

1. Center for Functional Cancer Epigenetics, Dana-Farber Cancer Institute, Boston, MA, USA.

2. Department of Medical Oncology, Dana-Farber Cancer Institute, Boston, MA, USA.

3. University of Oviedo, Instituto de Investigación Sanitaria del Principado de Asturias (ISPA), IUOPA, Oviedo, Spain and CIBERONC, Instituto de Salud Carlos III, Madrid, Spain.

4. Department of Data Science, Dana-Farber Cancer Institute, Boston, MA, USA.

5. Huntsman Cancer Institute, Dept. of Oncological Sciences, University of Utah, UT, USA

6. Department of Immunology, Harvard Medical School, Boston, MA, USA.

7. Blood Cell Development and Function Program, Fox Chase Cancer Center, Philadelphia, PA, USA.

8. Harvard Medical School, Boston, MA, USA.

9. Department of Cancer Immunology and Virology, Dana-Farber Cancer Institute, Boston, MA, USA.

10. Department of Oncologic Pathology, Dana-Farber Cancer Institute, Boston, MA, USA.

11. Breast Oncology Program, Dana-Farber Brigham Cancer Center, Boston, MA, USA.

12. Division of Breast Surgery, Department of Surgery, Brigham and Women's Hospital, Boston, MA, USA.

13. Department of Pathology, MD Anderson Cancer Center, Houston, TX, USA

14. Ludwig Center at Harvard and Laboratory of Systems Pharmacology, Harvard Medical School, Boston, MA, USA; Department of Systems Biology, Harvard Medical School, Boston, MA

15. Department of Pathology, Brigham and Women's Hospital, Boston, MA, USA.

16.Department of Breast Surgical Oncology, Division of Surgery, MD Anderson Cancer Center, Houston, TX, USA

17. Department of Medical Oncology, Sarah Cannon Cancer Center, Nashville, TN, USA.

18.Tennessee Oncology, Nashville, TN, USA.

19. Vanderbilt-Ingram Cancer Center, Vanderbilt University**,** Nashville, TN, USA.

20. Broad Institute of MIT and Harvard, Cambridge, MA, USA.

21. Department of Medicine, Brigham and Women's Hospital, Boston, MA, USA.

22. The BC Now Toby Robins Research Centre at the Institute of Cancer Research, London, UK and Ralph Lauren Centre for BC Research, Royal Marsden Hospital, London, UK

23. The Royal Marsden Hospital, London UK

#co-corresponding authors

Running title:

Endocrine therapy and SMAC-mimetics enhance immunogenicity

Keywords:

Estrogen receptor, BC, beta-2-microglobulin, NF-κB, SMAC-mimetic

Financial support: The work was conducted with support from the Maor Foundation (to O.M.F and R.J.), NIH support (RO1 CA237414-02 and K08 CA191058-05 to R.J), The DFCI Medical Oncology Award (to R.J.), and the Barr Award (to R.J.). ALW work is supported by grant #U54CA224076. The

PELOPS clinical trial was supported by Pfizer. M.C. was supported by an AIRC Fellowship for Abroad.

Corresponding authors:

Rinath Jeselsohn (Lead contact)

Dana-Farber Cancer Institute

450 Brookline Avenue

Boston, MA 02215

Tel: 617-623-3800

Fax: 617-632-1930

email: rinath_jeselsohn@dfci.harvard.edu

Otto Metzger

Dana-Farber Cancer Institute

450 Brookline Avenue

Boston, MA 02215

Tel: 617-623-3800

Fax: 617-632-1930

email: otto_metzger@dfci.harvard.edu

Conflict of interest statement: A.F.T is currently an employee at Bristol-Myers Squibb (BMS). I.L. is currently an employee at AbbVie. I.A.M. is currently an employee at Astra Zeneca. E.T.R. receives institutional research support from AstraZeneca, and educational honorarium from MJH Life Sciences.

S.M.T receives institutional research funding from AstraZeneca, Lilly, Merck, Nektar, Novartis, Pfizer, Genentech/Roche, Immunomedics/Gilead, Exelixis, Bristol-Myers Squibb, Eisai, Nanostring, Cyclacel, Odonate, and Seattle Genetics; has served as an advisor/consultant to AstraZeneca, Eli Lilly, Merck, Nektar, Novartis, Pfizer, Genentech/Roche, Immunomedics/ Gilead, Bristol-Myers Squibb, Eisai, Nanostring, Puma, Sanofi, Puma, Silverback Therapeutics, G1 Therapeutics, Athenex, OncoPep, Kyowa Kirin Pharmaceuticals, Daiichi-Sankyo, Ellipsis, Infinity, 4D Pharma, and Samsung Bioepsis Inc., Chugai Pharmaceuticals, BeyondSpring Pharmaceuticals, OncXerna, OncoSec Medical Incorporated, Certara, Mersana Therapeutics, CytomX, Seattle Genetics. D.A.Y. is a consultant for Bristol-Myers Squibb, Genentech/Roche, Eisai, Biotheranostics, Daiichi Sankyo/Lilly, Celgene, Novartis, NanoString Technologies and a receives research funding (institutional) from Macrogenics, Daiichi Sankyo, Clovis Oncology, AstraZeneca, Genentech/Roche, InventisBio, Syndax, Lilly, MedImmune, Pfizer, Eisai, Novartis, Medivation, Tesaro, Immunomedics, Abbvie, Merck, Oncothyreon and receives travel/accommodations/expenses from Genentech/Roche, Novartis and is a speakers'bureau for Genentech/Roche and Novartis. C.J.W is an equity holder of BioNTech. M.D. received honoraria from ad hoc ad boards or consultancies from: Lilly, Roche, Besins, Astrazeneca, and ROVI and receives income from the Institute of Cancer Research's Rewards for Discoverers scheme regarding Abiraterone. University of Utah may license the models described herein to for-profit companies, which may result in tangible property royalties to members of the Welm labs who developed the models (ALW and ZC). O.M.F. receives research funding (institutional) from Abbvie, Cascadian Therapeutics, Eisai, Pfizer, Roche/Genentech, and Susan G. Komen for the Cure, and is a consultant for Abbvie, G1 Therapeutics, and Groupo Oncoclinicas (Brazil), and receives honoraria from Roche (Brazil) and travel/accommodations/expenses from Grupo Oncoclinicas. R.J. received research funding (institutional) from Pfizer and Lilly and is a consultant for Carrick Therapeutics and GE Health. All other authors declare no potential conflicts of interest.

Author contributions:

Conceptualization: F.H.P, S.M.T, E.A.M, J.A, A.L.W., O.M, R.J.

Data curation: Q.J., N.T., T.S.

Formal Analysis: F.H.P, Y.X., D.R., A.F., X.Q., E.T.R, Y.H., G.S.

Funding acquisition: O.M, R.J.

Experiments: F.H.P., S.Sh., Z.N., M.Ca., M.Ch., K.L., A.N., C.G., Z.C.,J.R.L

Methodology: F.H.P, C.G, A.N, I.L., A.F.T., I.C, G.O., C.J.W., J.A.

Resources: W.F.S., I.B, I.A.M., D.A.Y., G.S., M.D.

Supervision: N.T., D.B, C.J.W., X.Q., H.L., S.Sa., J.G.P, S.M.T., M.D., A.L.W, O.M, R.J.

Visualization: F.H.P, D.R, T.A.

Writing – original draft: F.H.P, D.R, R.J.

Writing – review & editing: All authors

Acknowledgments:

We thank Dr Myles Brown and Dr Rafael Irizarry for the insightful discussions. We thank Ms. Cheri Fox and Mr. Stephen Koster for their important contributions.

Abstract:

Immunotherapies have yet to demonstrate significant efficacy in the treatment of hormone receptor positive (HR^+) breast cancer. Given that endocrine therapy (ET) is the primary approach for treating HR^+ breast cancer, we investigated the effects of ET on the tumor immune microenvironment (TME) in HR^+ breast cancer. Spatial proteomics analysis of primary HR^+ breast cancer samples obtained at baseline and after ET from patients enrolled in a neoadjuvant clinical trial (NCT02764541) indicated that ET upregulated B2-microglobulin and influenced the TME in a manner that promotes enhanced immunogenicity. To gain a deeper understanding of the underlying mechanisms, the intrinsic effects of ET on cancer cells were explored, which revealed that ET plays a crucial role in facilitating the chromatin binding of RelA, a key component of the NF-κB complex. Consequently, heightened NF-κB signaling enhanced the response to interferon-gamma, leading to the upregulation of β2-microglobulin and other antigen presentation-related genes. Further, modulation of NF-κB signaling using a SMAC-mimetic in conjunction with ET augmented T-cell migration and enhanced MHC-I specific T-cell mediated cytotoxicity. Remarkably, the combination of ET and SMAC-mimetics, which also block pro-survival effects of NF-κB signaling through the degradation of inhibitors of apoptosis (IAP) proteins, elicited tumor regression through cell-autonomous mechanisms, providing additional support for their combined use in HR^+ breast cancer.

Statement of Significance: Adding SMAC mimetics to endocrine therapy enhances tumor regression in a cell autonomous manner while increasing tumor immunogenicity, indicating that this combination could be an effective treatment for HR^+ breast cancer patients.

Introduction

Immune checkpoint inhibitors (ICIs) and other immune therapies revolutionized the treatment paradigms of several malignancies (1). However, the use of ICIs has been limited in BC and mostly studied in the triple-negative BC (TNBC) subtype(2, 3). ICIs have shown marginal efficacy in HR+ BC, and there are no approved immunotherapy regimens in this BC subtype. Nonetheless, several studies demonstrated a signal of clinical benefit in a limited number of patients (4-6), highlighting the potential utility of ICIs and unmet need to identify strategies to harness the immune system for the treatment of a broader population of patients with HR+ BC.

The inherent resistance to ICIs in HR+ BC is attributed to the low tumor mutational burden, low percentage of stromal tumor infiltrating lymphocytes (sTIL), and low PD-L1 expression (7-9). Antigen presentation is required for the activation of cytotoxic CD8+ TILs and inadequate antigen presentation is another mechanism of tumor immune escape and resistance to ICIs (10). The major histocompatibility complex class I (MHC-I) is a key component of the antigen presentation machinery, responsible for the presentation of intracellular peptide antigens to the cell surface for specific cytotoxic T-cells recognition. High MHC-I expression correlates with better responses to ICIs in lung cancer and melanoma (10, 11). The MHC-I complex is a heterodimer consisting of two polypeptide chains including α and β_2-microglobulin (B2M). The α chain is polymorphic and encoded by an HLA gene (*HLA-A/B/C*), whereas the B2M subunit, encoded by the *B2M* gene, is not polymorphic. In cancers, MHC-I expression is mainly induced by the type II interferon, interferon gamma (IFN-γ), which is secreted primarily by T-cells and natural killer (NK) cells and signals through the JAK-STAT pathway. A link between estrogen receptor α (ER) signaling and antigen presentation was demonstrated in a study that showed an inverse correlation between MHC-I and ER expression in primary BC and normal

breast tissue (12). Moreover, in metastatic HR+ BC, higher ER signaling was associated with reduced antigen presentation and ICI resistance (13). Thus, there is evidence for the role of ER in modulating antigen presentation and sensitivity to ICIs, however, the underlying mechanisms of these effects remain elusive.

Previous studies showed that estradiol (E2) impacts innate immune signaling pathways and myeloid cell development (14, 15). Additionally, several studies investigated the effects of ER signaling on the TME in tumors that are not ER dependent (16, 17). In this study, we sought to investigate the effects of ER blockade on the TME and tumor cell response to immune stimuli and antigen presentation in ER+ BC with the aim to identify strategies to increase the immunogenicity of HR+ BC.

Material and Methods

Clinical Trial design, Tumor biopsies and Compliance with Ethical Standards:

Palbociclib and ET for Lobular BC Preoperative Study (PELOPS) was a multi-center, randomized, open label phase II neoadjuvant clinical trial that enrolled patients with resectable early stage, treatment naïve hormone receptor positive, HER2 negative BC. The study included two parts and two patient cohorts based on the menopausal status (post-menopausal and pre-menopausal). The first part was a window of opportunity study in which the post-menopausal patients were randomized 1:1 to two weeks of treatment with tamoxifen (20 mg) versus letrozole (2.5 mg). In the second part of the study, the treatment part, the post-menopausal patient cohort re-randomized 2:1 to palbociclib plus letrozole versus letrozole alone. The pre-menopausal patients were randomized 2:1 to tamoxifen with lupron and palbociclib versus tamoxifen and lupron. Randomization was stratified by histological subtype (IDC and ILC, mixed pathology was categorized at IDC), lymph node status, and tumor size. Main eligibility criteria included: Stage I to III histologically confirmed invasive carcinoma of the breast. A minimum

tumor size of at least 1.5 cm determined by physical exam or imaging (based on the larger measurement), histologically confirmed hormone receptor positive (ER and/or PR), HER2 negative, early invasive BC. Cut-off values for positive/negative staining was in accordance with current ASCO/CAP (American Society of Clinical Oncology/College of American Pathologists) guidelines. Participants underwent a research biopsy at baseline and day 15. Core biopsies were obtained and for snap frozen samples and formalin fixed paraffin embedded (FFPE) blocks. FFPE tissue blocks, and/or cut slides were collected from the surgical excision at the end of the study. The clinicopathologic characteristics of the 111 patients in this analysis were comparable to the entire study population, and the clinical characteristics were well balanced between the treatment arms. The study was conducted in accordance with the International Conference on Harmonization Good Clinical Practice Standards and the Declaration of Helsinki. Institutional review board (IRB) approval was obtained at Dana-Farber/Harvard Cancer Center (DF/HCC) (Dana-Farber/Harvard Cancer Center Protocol 16-052). The study was registered in ClinicalTrials.gov (NCT02764541). The DF/HCC Data and Safety Monitoring Committee, which is composed of clinical specialists with experience in oncology and who had no direct relationship with the study, reviewed and monitored toxicity and accrual data from the study. Participants provided written informed consent prior to the performance of any protocol specific procedures or assessments. The study was an investigator-initiated trial funded by Pfizer. Palbociclib was supplied by the manufacturer (Pfizer). The funder had no role in data collection, data analysis or data interpretation. The clinical primary end points of the study were: two primary end points: 1. Window of opportunity part: compare the changes in Ki67 (fold change of Ki67 on log scale) between tamoxifen treatment and letrozole. 2. Treatment part: evaluate the effect of including palbociclib with ET compared to ET alone on pathologic response among all patients (based on RCB index. These results will be reported in a separate publication.

Digital Spatial profiling data generation

Digital spatial profiling (DSP, NanoString) was performed as described previously (18). Tissue slides were stained with a multiplex panel of protein antibodies that have a photocleavable indexing oligonucleotide, which enables subsequent readouts. Regions of interest (ROIs) were selected on a DSP instrument and illuminated using UV light. Released indexing oligonucleotides from each ROI were collected into designated wells on a microplate for indexing of each ROI for nCounter and readout by direct protein hybridization. ROIs were collected after review by a pathologist to assure collection of ROIs with invasive cancer cells.

Digital Spatial Profiling Analysis

NanoString DSP data were normalized using lane-specific External RNA Controls Consortium (ERCC) normalization and sample-specific housekeeping normalization using the controls Ms IgG1, Ms IgG2a, Rb IgG, GAPDH, Histone H3, and S6. Individual observations were filtered to remove outliers and poor-quality samples and were log2 transformed for all subsequent analyses. Hierarchical clustering with complete linkage was performed on the 25 proteins with the largest variance across all observations, and principal components was run on the centered and scaled protein expression matrix. Differential protein expression was tested for all non-control proteins using linear mixed effect models with protein expression used as a univariate response, a single categorical variable used as a fixed effect covariate, and a patient-specific random intercept term to account for multiple expression measurements taken per patient. Sample sizes reported are the number of patients, not the total number of measurements. Separate models were run for each subset of patients and fixed effect analyzed. The models were fitted using the R package lme4 (19), and tests for significance of fixed effects were calculated using the R package lmerTest (20) using t-tests with a Satterthwaite approximation for degrees of freedom. P-values were adjusted for multiple testing using the Benjamini-Hochberg procedure. A False Discovery Rate (FDR) threshold of 5% was used to report differentially expressed

proteins, and log2 fold changes were calculated based on the un-log2 transformed normalized data. DSP trajectories of individual proteins between timepoints for each patient were calculated by taking the average expression of that protein by patient at each fixed timepoint. Pearson correlations were calculated between average DSP Ki-67 measurements per patient and shifted log2 IHC Ki-67 measurements (log2(Ki-67% + 1%)), and two-sided tests of the correlation coefficient were performed. Since previous studies showed that the spatial location of the immune cells may affect the activity and expression profiles of specific immune cell types (21), we compared the immune regions that were proximal and in direct contact to the invasive cancer cells, the immune regions distal to the invasive cancer cells (within the tumor borders) and immune regions that were between (intermediate) these two locations. Principal components analysis did not segregate these spatially different immune regions (N = 108) and therefore, we did not distinguish between these regions in subsequent analyses (Supplementary Fig. S1A).

Immunohistochemistry studies and TILS analysis

Dual immunohistochemical staining of Ki-67 and Cytokeratin was conducted on 4µm FFPE sections, using both Bond Polymer Refine Kit and Bond Polymer Refine Red kit in Leica Bond RX system. The slides were deparaffinized, and heat-mediated antigen retrieval was performed with EDTA buffer (pH 9.0). The slides were incubated with the antibody against Cytokeratin (CAM5.2, Cell Marque) at 1:5,000 dilution for 30 minutes at room temperature, and antigen-antibody reaction was visualized with DAB chromogen. The slides were sequentially incubated with Anti-Ki-67 antibody (BIOCARE MEDICAL Cat# CRM 325, RRID:AB_2721189) at 1:100 dilution for 60 minutes at room temperature and visualized using Fast Red chromogen. Omission of the primary antibody was used as a negative control. Whole slide images were acquired from stained slides using a Vectra 3.0 Automated Quantitative Pathology Imaging System (Akoya Biosciences) and analyzed using Halo Image Analysis

platform (Indica Labs). Image annotations were performed by a pathologist, the areas containing invasive carcinoma were included in image analysis. We utilized the Halo image software, employing an algorithm using color deconvolution to separate brown and red chromogenic stains for analysis, trained to identify the invasive tumor cells based on Cytokeratin masking, and subsequently completed cell segmentation. The threshold for Ki-67 was set based on the staining intensity of visualization of Red in nucleus staining and applied to the whole annotated image; tumor cells with the intensity above the setting threshold were defined as Ki-67 positive. TILS were analyzed by a pathologist and scored based on the International TILs working group method (22).

Cell Lines and Cell culture

MCF7 (RRID:CVCL_0031), T47D (RRID:CVCL_0553), CAMA-1 (RRID:CVCL_1115), ZR75.1 (RRID:CVCL_0588), and HEK-293 (RRID:CVCL_0045) cells were purchased from the ATCC and authenticated using standard short tandem repeat analysis in 2019. DOX-inducible ER Y537S mutant and WT-ER cells as well as *ESR1* Y537S knock-in mutant cells were previously generated in MCF7 cells (23). MCF7, CAMA-1, and HEK293 were cultured in DMEM supplemented with 10% FBS, 1% l-glutamine, and 1% penicillin and streptomycin (P/S). T47D and ZR75.1 were cultured in RPMI 1640 supplemented with 10% FBS, 1% l-glutamine, and 1% P/S. All cells were used at low passage numbers and were tested for Mycoplasma using the MycoAlert Mycoplasma Detection Kit (Lonza). For hormone-depleted (HD) conditions, cells were kept in phenol-red free medium supplemented with 10% heat-inactivated charcoal-stripped (CS)-FBS and 1% P/S for 72h. All cell lines were incubated at 37°C in 5% CO_2. To created MCF7_NY-ESO-1 cells, MCF7 cells were transduced with pHAGE vector containing NY-ESO-1 sequence and ZsGreen protein (NY-ESO-1_Luc_ZsGreen_pHAGE). To select NY-ESO-1 expressing cells, MCF7 cells transduced with NY-ESO-1 vector were sorted twice based on ZsGreen expression. Plasmid NY-ESO-1_Luc_ZsGreen_pHAGE was a gift from Kai Wucherpfening´s

lab (24). Compounds used for cell lines treatments: Beta-Estradiol (Sigma Aldrich E2758), Fulvestrant (Sigma Aldrich I4409), Birinapant (Selleckchem, 7015) and ARV-471 (MEDCHEM EXPRESS LLC, HY-138642.

Flow cytometry analysis

Treatment conditions for flow cytometry analysis were conducted as follows, unless specified otherwise: BC cell lines were grown in the presence of estradiol 10 nM (E2), in hormone deprived conditions (HD) or treated with either vehicle, fulvestrant, birinapant or the combination for a total of 72 hours. For IFNg stimulation studies, after 48 hours, treatments were refreshed with or without IFNg (10 ng/mL) for last 24 hours prior to flow cytometry analysis. Before the analysis, tumor cells or T-cells were suspended in FACS staining buffer (1% BSA, 1 mM EDTA in PBS) and stained with fluorochrome-conjugated antibodies against combinations of the following surface human antigens: HLA-ABC ((BioLegend Cat# 311415, RRID:AB_493134), PDL1/CD274 (BioLegend Cat# 329707, RRID:AB_940358) and HA-tag (BioLegend Cat# 901509, RRID:AB_2565072). Cell viability was determined using propidium iodide exclusion (Life Technologies, P3566) or DAPI (Thermo Fisher, 62248). Flow cytometric data were acquired using an LSR Fortessa cytometer (BD) and analyzed with FlowJo software version 10 (FlowJo LLC).

Lentivirus production

The day before transfection, HEK-293FT cells were plated in 6-well plates at 40-60% confluence. Transfection was performed using 6 µl per well of X-tremeGENE HD (Sigma-Aldrich). For each well: 0.4 µg VSVG, 1 µg psPAX2 and 3 µg of the vector of interest were added to 1 mL of Opti-MEM (Life Technologies) along with the transfection agent. After overnight culture, media was changed with 3 mL of DMEM containing 20% FBS for virus collection. Supernatant was harvested after 48h and filtered

with 0.45 nm filters. Virus particles were either used right away or frozen in aliquots for future transductions.

T-cell isolation and transduction

PBMCs were isolated from healthy donor's blood using density gradient medium (Lymphoprep™, Stemcell Technologies) and SepMate™ PBMC Isolation Tubes (Stemcell Technologies). T-cells were isolated from PBMCs using EasySep™ Human T Cell Isolation Kit (Stemcell Technologies). Isolated T cells were seeded in non-treated 24 well plates and activated in the presence of 30 IU/ML of IL2 (Stemcell Technologies) and biotinylated antibodies against human CD2, CD3, and CD28 (Human T Cell Activation/Expansion Kit, Miltenyi) in RPMI 1640 containing 10% FBS, 1% l-glutamine, and 1% P/S and streptomycin.

Freshly activated T-cells were transduced with a recombinant T cell receptor (TCR) specific for the NY-ESO-1 antigen (NY-ESO-1:157–165 epitope) presented in an HLA-A* 02-restricted manner. Briefly, between 0.5 to 1 million activated T-cells were plated in non-culture treated 24 well plates in the presence of 30 IU/mL of IL-2 and 8 ug/mL of Polybrene. Viral particles were added to the mixture and cells underwent spin infection (800G for 2 hours at 37 C. After spin infection, T-cells were incubated with viral particles for 3 days. NYESO TCR expression was measured by flow cytometry after 5 days using HA-tag antibody (BioLegend Cat# 901509, RRID:AB_2565072) and sorted for coculture experiments. Activated TCR+ T-cells were then cultured at a density of 0.7–1.0 x 10^6 cells per ml for 10-14 days and used for coculture experiments. All PBMCs and lymphocytes used were obtained from leukapheresis collars from healthy donor's at Crisom Core at BWH on an IRB-approved protocol (DFCI protocol 17-684). Recombinant TCR specific for the NY-ESO-1 antigen was a gift from Kai Wucherpfening´s lab.

Chromatin Immunoprecipitation (ChIP)-Sequencing

ChIP experiments were conducted as described previously (23) and were done in duplicates. MCF7 cells were grown in HD conditions for three days (HD) or in the presence of 10nM of estradiol for three days (E2) with or without IFN-γ stimulation (10 ng/mL) for 1 h. Chromatin from approximately 1 x 10^7 fixed cells was sonicated to a size range of 200-300 bp in a Covaris E220 instrument in 1 mL AFA Fiber milliTUBEs. Solubilized chromatin was subjected to immunoprecipitation overnight with RELA antibody (Cell Signaling Technology Cat# 8242, RRID:AB_10859369) and bound to protein A and protein G beads (Life Technologies). A fraction of the sample was not exposed to antibody to be used as control (input). The samples were reversed crosslinked, treated with proteinase K, and DNA was extracted. DNA was then submitted for library preparation and sequencing to the Molecular Biology Core Facilities (MBCF) at Dana-Farber Cancer Institute. ChIP-seq analysis was performed as previously reported (23, 25). ChIP reads were aligned to the hg19 genome assembly using BWA (26) and ChIP-seq peaks were called using MACS 2.0 (27, 28) . For differential analysis, bed-files were merged using bedops (29) and then DEseq2 was used to assign differential intensities and statistics. Differential binding sites was determined by filtering out insignificant peaks (adjusted p-value<0.05) and then determining log2FC values between samples for each region using a log2 FC >0 or <0. Unsupervised sample-to-sample correlation analysis was done using Euclidean distance and Ward's method. Analysis was done using the CoBRA workflow (30), which included motif analysis.

ATAC sequencing

Assay for Transposase-Accessible Chromatin sequencing (ATAC-seq) was performed to study global chromatin accessibility for non-IFN-γ stimulated conditions, MCF7 cells were grown in estrogen deprived conditions (HD) or in the presence of estradiol 10 nM for 3 days. For IFN-γ stimulated conditions, MCF7 cells were grown in HD or in the presence of estradiol 10 nM for 48h and then

treated with 10 ng/mL of IFN-γ for 24h. ATAC-seq was performed as previously described (31, 32). Briefly, cells were resuspended in 1 mL of cold ATAC-seq resuspension buffer (RSB; 10 mM Tris-HCl pH 7.4, 10 mM NaCl, and 3 mM MgCl2 in water) and centrifuged. Cell pellets were then resuspended in ATAC-seq RSB (0.1% NP40, 0.1% Tween-20, and 0.01% digitonin) and incubated on ice. After lysis, ATAC-seq RSB containing 0.1% Tween-20 (without NP40 or digitonin) was added. Nuclei were centrifuged and then were resuspended in 50 µl of transposition mix (25 µl 2× TD buffer, 2.5 µl transposase (100 nM final), 16.5 µl PBS, 0.5 µl 1% digitonin, 0.5 µl 10% Tween-20, and 5 µl water). Transposition reactions were incubated at 37 °C for 30 min. Reactions were cleaned up with Zymo DNA Clean and Concentrator 5 columns. For ATAC-seq data analysis, we used Burrows-Wheeler Aligner (BWA) (33) to map sequencing reads to the reference genome and MACS2 (27) for peak calling. DESeq2 (34) was applied to identify the differentially accessible regions with or without IFN-γ treatment from ATAC-seq data and significant differences were based on a Log2 FC >0.5 or <0.5, q-value <0.05.

RNA sequencing

MCF7 cells were grown in hormone deprived conditions or in the presence of estradiol, 10nM for 72h hours. RNA was extracted after 6h, 12h, 24h and 48h of IFN-γ stimulation. For each experiment, total RNA was isolated using a RNeasy Mini Kit (Qiagen, 74134) in triplicates. RNA concentrations were measured by NanoDrop and quality of RNA was determined by a Bioanalyzer. For all cell line studies, samples were analyzed in at least duplicates. RNA-seq libraries were made using the TruSeq RNA Sample Preparation Kit (Illumina). Samples were sequenced on an Illumina Nextseq500. The RNA-seq analyses were performed using the VIPER analysis pipeline (35, 36). Alignment to the hg19 human genome was done using STAR v2.7.0f followed by Transcript assembly using cufflinks v2.2.1(37) and RseQC v2.6.2 (38). Differential Expression Analysis was done using DEseq2 v1.18.1 (34). Significnat

changes were based on a Log2FC> 0.5 or <0.5, adj-p-value<0.05, DEseq2 GSEA analysis was performed using the Broad GSEA Application (39). For TCGA analyses, we used Gene Set Variation Analysis, which is a non-parametric method for estimating variation of pathways over a sample population in an unsupervised manner (40).

Binding and Expression Target Analysis (BETA)

To identify the putative genes that are immediate transcription targets of RELA we used the BETA tool (41). This tool consists of three tools including BETA minus, BETA basic and BETA plus. In this manuscript we used BETA minus and BETA basic. In BETA minus transcription factor target gene prediction is based on a regulatory score applying ChIPseq data only. In BETA basic transcription factor activating, or repressive function is predicted based on ChIPseq and RNAseq data using the Kolmogorov-Smirnov test. For no IFN-γ conditions, we used RNA-seq and RELA ChIP-seq data from MCF7 cells grown in HD or E2 for 3 days. For IFN-γ conditions, we used RNA-seq data from MCF7 cells grown in HD or E2 for 3 days stimulated with IFN-γ for 6 hours and RELA ChIP-seq data from MCF7 cells grown in HD or E2 for 3 days stimulated with IFN-γ for 1 hour. The RelA_HD gene set was derived by overlapping the genes that were identified by BETA basic to be regulated by RelA in HD conditions and are upregulated in HD conditions compared to E2 conditions by RNAseq (Log2FC> 0.5, adj-p-value<0.05, DEseq2)

RELA CRISPR Knock-outs (KOs)

To validate the role of RELA in the response to IFN-y, we performed CRISPR-Cas9–mediated deletion of RELA in multiple cell lines. Briefly, Cas9-expressing cell lines (RRID:Addgene_68343) were transduced with a guide RNA (gRNA) designed to match RELA exon sequence

(RRID:Addgene_67974) or with the empty vector as a control. We created two different knock out cellular populations using two different gRNAs for RELA (RELA KO1 and RELA KO2). Knock outs were validated by mRNA and protein levels.

RELA KO1 guideRNA: GAAGATCTCATCCCCACCG

RELA KO2 guideRNA: CTACGACCTGAATGCTGTG

Cytokine profiling

Multiplex assays were performed utilizing the bead-based immunoassay Human Cytokine/Chemokine Magnetic Bead Panel (catalog no. HCYTMAG-60K-PX30) on a Luminex MAGPIX system (Merck Millipore). Conditioned media concentration levels (pg ml−1) of each protein were derived from five-parameter curve-fitting models. Lower and upper limits of quantitation were imputed from standard curves for cytokines above or below detection. For non-IFN-γ stimulated conditions: MCF7 cells and MCF7 *ESR1* Y537S knock-in mutant cells were grown in estrogen deprived conditions (HD) or in the presence of estradiol10nM (E2) for 3 days. For IFN-γ stimulated conditions, MCF7 cells and MCF7 *ESR1* Y537S knock-in mutant cells were grown in estrogen deprived conditions (HD) or in the presence of estradiol 10 nM (E2) for 72h and stimulated with 10 ng/mL of IFN-γ for the last 24h.

Proteome Profiler Human XL Cytokine Array Kit (ARY022B—R&D System) was used to analyzed levels of cytokines, chemokines, and growth factors from conditioned media of BC cells following the manufacturer's instructions. MCF7 cells were pretreated with vehicle, fulvestrant (10nM), birinapant (100nM) and the combination of both drugs for 48h, FBS containing media was then removed and IFN-γ was added along with the treatments in a FBS free media for 24h along when conditioned media was collected.

Patient Derived Xenograft Studies

Female 5–6-week-old NRG mice (Jackson labs stock #007799) were implanted with HCI-011 PDX tumor fragments using a previously described protocol with estrogen supplementation (42). When tumors reached approximately 100 mm^3, mice were randomized into treatment or control groups. Mice received either vehicle control (15% captisol IP, 3x/week for 5 weeks), birinapant (20 mg/kg IP, 3x/week for 5 weeks), fulvestrant (200 mg/kg subQ, 1x/week for 5 weeks), or the combination of birinapant and fulvestrant at the same doses as single agents. For birinapant treatment, birinapant (Medchem Express, HY-16591) was dissolved in 15% captisol at a concentration of 2 mg/ml (made fresh every time), and 100ul/10g mouse body weight was injected intraperitoneally. For fulvestrant treatment, 250 mg of fulvestrant (Selleck Chemicals, S1191) was dissolved in 0.5 ml DMSO, incubated at 37^oC for 15 min, then diluted 1:20 with corn oil to give final concentration of fulvestrant of 25 mg/ml (made fresh every time). 80ul/10g mouse body weight was injected subcutaneously. Animal experiments were all conducted in compliance with institutional guidelines and regulations after approval from the University of Utah Institutional Animal Care and Use Committee, under protocol 21-06008.

T-cell co-culture assay

MCF7 NY-ESO-1 and primary T-cells expressing NY-ESO-1 TCR were used for co-cultured assays. One day before co-culture, MCF7 NY-ESO-1 cells were seeded at specific density on 24 well plates in the same media as the T-cells and treated overnight with the specified conditions. The next day, NY-ESO-1_TCR+ T-cells were added to the plates at 1:1 effector:target ratio and co-cultured for 12-16 hours. After this time, T-cells were carefully washed away by 2x phosphate-buffered saline (PBS) washes. Hoechst was used for nuclear staining and propidium iodide was used for staining dead cells.

Tumor cells were counted using the Celigo image Cytometer instrument (Nexcelom, RRID:SCR_018808).

Proliferation assays

BC cells were plated in 24 well plates at a density of 8000 cells per well. At indicated time points, cells were counted using the Celigo image Cytometer (Nexcelom, RRID:SCR_018808). Hoechst was used for nuclear staining and propidium iodide was used for staining dead cells. Fulvestrant and birinapant were used for the growth and synergy studies. Synergy score was calculated using SynergyFinder and ZIP synergy scoring (43).

Immunoblotting

Cells were lysed in RIPA buffer (Thermo Fisher, 89900) supplemented with phosphatase and protease inhibitors and subjected to SDS-PAGE. Antibodies used were ERa (Santa Cruz Biotechnology Cat# sc-543, RRID:AB_631471), RelA/p65 (Cell Signaling Technology Cat# 6956, RRID:AB_10828935), phospho-RelA Ser536 (Cell Signaling Technology Cat# 3033, RRID:AB_331284), GAPDH (Santa Cruz Biotechnology Cat# sc-25778, RRID:AB_10167668), RelB (Cell Signaling Technology Cat# 10544, RRID:AB_2797727), NF-κB1 p105/50 (Cell Signaling Technology Cat# 12540, RRID:AB_2687614), NF-κB2 p100/52 (Cell Signaling Technology Cat# 3017, RRID:AB_10697356), IRF1 (Cell Signaling Technology Cat# 8478, RRID:AB_10949108), STAT1 (Cell Signaling Technology Cat# 9176, RRID:AB_2240087), phospho-STAT1 Tyr701 (Cell Signaling Technology Cat# 9167, RRID:AB_561284), MHC-I (Thermo Fisher Scientific Cat# MA5-11723, RRID:AB_10985125), PDL1 (Abcam Cat# ab228415, RRID:AB_2884993).

3D Migration assay

Immune cell infiltration was assessed as previously described (44). Briefly, MCF7 cell spheroids were generated by seeding 5 x 105 cells in suspension in an Ultra-low attachment (ULA) dish for 48h hours. MCF7 spheroids were treated for 48h with vehicle (DMSO), fulvestrant (10nM), birinapant (100nM) and the combination. Samples were then pelleted and resuspended in type I rat tail collagen (Corning) at a concentration of 3 mg/mL following the addition of 10x PBS with phenol red and pH adjustment using NaOH. pH 7.0–7.5 was confirmed using PANPEHA Whatman paper (Sigma-Aldrich). Cells and collagen were kept on ice to prevent polymerization. The spheroid-collagen suspension was then injected into the central gel region of the 3D DAX-1 3-D microfluidic cell culture chip (AIM Biotech). Microfluidic devices were utilized as previously described, with a central region containing the cell-collagen mixture in a 3D microenvironment (30,000 cells in 10 μL), flanked by two media channels located on either side. After injection, collagen hydrogels containing cells were incubated for 40 minutes at 37°C in humidity chambers, then hydrated with culture media, with labeled CD8+ T-cells (E:T ratio 2:1) added to one of the side channels. CD8+ T-cells were labeled with CellTrace Red Stain (Thermo Fisher Scientific) following the manufacturer's instructions. Treatments were refreshed along with the culture media. After 72 hours of incubation, images were captured on a Nikon Eclipse 80i fluorescence microscope equipped with Z-stack (Prior) and CoolSNAP CCD camera (Roper Scientific). Image capture and analysis were performed using the NIS-Elements AR software package. Whole device images were achieved by stitching in multiple captures. Quantification of immune cell infiltration into the 3D tumor microenvironment was performed by measuring the total cell area of cell tracker dye in the entire gel region.

Data availability

The whole-genome sequencing, RNA-seq, ChIP-seq and ATAC-seq data were all submitted to GEO accession number GSE214054. RNAseq and clinical data from the TCGA BC cohort (45) were

downloaded from https://portal.gdc.cancer.gov/ and from reference (46) for the BC biopsies pre and post neoadjuvant AI treatment. All other raw data are available upon request from the corresponding author.

Results

ET in HR+ primary BC increases the expression of B2M and STING

To investigate the effects of ET on the TME and the invasive cancer epithelial cells (ICECS) in HR+ BC, we performed multi-plex spatial proteomic characterization of primary BCs. We assayed 294 primary BC tissue samples from 111 patients with primary ER+/HER2-negative BC who participated in the neoadjuvant Palbociclib and ET for Lobular BC Preoperative Study (PELOPS), including samples from baseline, on treatment (day 15), and surgery time points (Fig. 1A). The clinicopathological characteristics of the patients are detailed in Supplementary Table S1. Regions of interest (ROIs) were selected based on geographical and phenotypic characteristics. Pan-cytokeratin and CD45 immunofluorescence was used to select regions of ICECs and immune regions (regions of sTILS) for the quantification of tumor and immune related proteins (Fig. 1B and Supplementary Table S2 and S3). Unsupervised hierarchical clustering of all ROIs to look for broad patterns within and between patients segregated the immune from ICECs regions (Supplementary Fig. S1B). Comparison of the immune and ICECs ROIs at the 3 timepoints showed upregulation of cell surface markers of T and B lymphocytes in the immune regions, while ICECs regions exhibited upregulation of ER, Pan-CK, EpCAM, and progesterone receptor (PR) (Supplementary Fig. S1C-1F and Supplementary Table S4).

Next, we examined the effects of ET. In the post-menopausal patients randomized to the window of opportunity part of the trial, after two weeks of tamoxifen or letrozole treatment there were no

significant expression changes in the sTIL regions. In contrast, in the ICECS regions, tamoxifen treatment resulted in a significant increase in PR and a trend towards a decrease in Ki-67 (Supplementary Fig. S1G-1H and Supplementary Table S4), while letrozole treatment led to a significant decrease in Ki-67 and PR (Supplementary Fig. S1I-1J and Supplementary Table S4). This is consistent with previous studies showing greater suppression of Ki-67 with an aromatase inhibitor (AI) compared to tamoxifen after two-weeks of treatment (47). Of note, there was a strong correlation between Ki67 levels and the ratio of Ki-67 at 2 weeks/baseline comparing Ki67 quantified by DSP and immunohistochemistry (Supplementary Fig. S1K-1N). Thus, these results provide evidence that the analysis of selected regions can represent the entire section.

After 24 weeks of ET, we detected significant changes in the expression of several immune related proteins in the ICECs regions, including upregulation of STING (stimulator of interferon genes), B2M, CD40, TIM3, B7-H3 and CTLA4, and downregulation of TNFR and CD137 (Fig. 1C-1E and Supplementary Table S5). In addition, we observed an increase in ER expression, likely an adaptative response to ER signaling blockade, and a decrease in PR and Ki-67 (Fig. 1E). In the immune regions, (Fig. 1F-1H and Supplementary Table S6) there was also a significant increase in B2M, STING, and CD40, and decrease in CD137. Additionally, there were multiple changes unique to the immune regions, such as an increase in the CD3 and the CD4 T-cell markers and a decrease in the regulatory T-cell (T-reg) marker, FOXP3 (Supplementary Fig. S2A-2F).

To validate our results in an independent patient cohort we turned to the transcriptomic data from the NEOAI study, a retrospective study of patients with primary ER+/HER2- BC who received neoadjuvant treatment with an AI for at least 4 weeks. Thirty-two of the proteins tested in our study overlapped with the nanostring mRNA panel that was applied in NEOAI (Supplementary Table S7). Because the majority (63%) of these proteins were significantly upregulated in the immune regions

compared to the cancer cell regions, we used the expression levels of the immune regions. Indeed, we observed a significant correlation between the gene expression changes after AI treatment in the NEOAI study and the protein expression changes after letrozole treatment in PELOPS (Supplementary Fig. S2G).

To assess the relative abundancies of the immune cell populations and how they are impacted by ET, we focused on the expression levels of immune cell surface markers. Analysis the ICECs and the immune regions separately at each of three timepoints revealed unequal expression of the immune cell surface markers within each region subtype (Fig. 2A-2F) and differences between the ICECs and the immune regions. In the ICECs regions at baseline, the most abundant markers of immune cells infiltrating the tumor cells were the pan-macrophage (CD68) and dendritic cell (CD11c) markers, while the least abundant were markers of Tregs (FOXP3) and active neutrophils (CD66b) (Fig. 2A). This ranking persisted after two and 24 weeks of ET (Fig. 2B-2C). In the immune regions at baseline (Fig. 2D) and after 2 weeks of ET (Fig. 2E) the most abundant immune cell surface marker was the CD8 T-cell marker, followed by the CD68 macrophage marker, which is consistent with previous studies showing that the most abundant immune cells in BC, including ER+ BC, are T-cells and myeloid cells (48). After 24 weeks of ET, the most abundant immune cell surface markers were CD3 and CD4, followed by CD8 (Fig. 2F). CD4+ T-cells are important for the function of CD8+ T-cells (49), and a higher CD4:CD8 ratio has been shown to be important in sustaining the function of adoptively transferred T-cells (50), suggesting that this change may favorably impact immunogenicity.

As expected in ER+ BCs, the median fraction of sTIL in the entire slide was low (Supplementary Table S1). While there were no changes in the fraction of sTIL after two weeks of ET (Fig. 2G), after 24 weeks of treatment at the time of surgery there was a significant increase in the fraction of sTIL (Fig. 2H). Although, the sTIL fraction was still relatively low at this time point (<0.3). The increase in sTIL

and the changes in the expression of immune related proteins did not correlate with Ki67 suppression at two weeks, a biomarker of response to ET, suggesting that these changes were not dependent on tumor response to treatment (Supplementary Fig. S2H-2I). In keeping with the increase in the sTIL fraction that we detected, in a separate cohort of ER+/HER2 negative primary BCs for which RNAseq data was available (46), neoadjuvant treatment with an AI resulted in an increase in the expression of the gene signature of cytotoxic T-cell accumulation (51) (Fig. 2I).

To study the associations between ER signaling and immune related pathways in a separate cohort of ER+ BCs, we utilized the bulk transcriptomic data from The Cancer Genome Atlas (TCGA). We divided the ER+ BCs (n=802) to quartiles based on *ESR1* mRNA levels. Gene set enrichment analysis (GSEA) comparing tumors in the 1st versus 4th quartile confirmed that the tumors with higher expression of *ESR1* mRNA levels exhibited higher ER transcriptional activity (Fig. 2J). We next tested the association between *ESR1* mRNA levels and the expression of signatures that predict benefit from ICIs applying gene set variation analysis (GSVA) (40). High *ESR1* mRNA was associated with increased expression of a signature of ICI resistance (52) (Fig. 2K) and T-reg accumulation (52) (Fig. 2L). Conversely, lower *ESR1* mRNA expression was associated with increased cytotoxic T cell accumulation (51) (Fig. 2M). These findings are consistent with the analysis of the PELOPS biopsies, where we observed increased expression of B2M and CD4, increased TIL fraction, and decreased expression of FOXP3 after ET.

Previous studies demonstrated that CDK4/6i can increase the immunogenicity and response to ICIs in models of BC and other cancer types by influencing the tumor cells and TME through several mechanisms (53, 54). In our study, we also analyzed the effects of 24 weeks of treatment with palbociclib and ET in HR+ BCs. The most significant changes at the protein level in the ICECS regions (N = 79) included upregulation of STING, B2M and the immune checkpoint TIM-3 (Supplementary

Fig. S3A). In the immune regions (N = 77), the most significant changes were increased expression of B2M and CD40 (Supplementary Fig. S3B). Comparison of the protein changes induced by ET alone versus ET in combination with palbociclib revealed a high overlap, and nearly all proteins upregulated by ET were also upregulated by the treatment combination. In contrast, there were additional proteins uniquely upregulated by the addition of palbociclib, including granzyme B, PD-L1, HLA-DR, and others (Supplementary Fig. S3C-3D). Several proteins were uniquely down regulated in ET alone, such as FOXP3, PD-1, and IDO-1 (Supplementary Fig. S3E-3F). Taken together, these results indicate that although the effects of ET as monotherapy and in combination with palbociclib differ, both treatments impact the innate and adaptive immune pathways in a manner that overall favors increased immunogenicity.

Estrogen receptor signaling impedes MHC-I expression

Since the upregulation of B2M in the ICECs regions in ER+ BCs was among the most significant changes after ET, we sought to investigate the cancer cell intrinsic effects of ER perturbation on MHC-I expression in ER+ BC cell lines (MCF7, T47D, CAMA1 and ZR75.1). To this end, ER+ BC cells were cultured in hormone deprived (HD) conditions or in the presence of estradiol (10nM) for 72 hours (h), with IFN-γ stimulation during the last 24h prior to flow cytometry analysis of MHC-I levels (Supplementary Fig. S4A). Baseline levels of MHC-I varied between the different cell lines, but in all cells the expression was induced by IFN-γ stimulation. Strikingly, the IFN-γ induced upregulation of MHC-I was lower in E2-treated compared to HD conditions in all cell lines (Fig. 3A-3E). These results were confirmed by Western blot analysis, which demonstrated that MHC-I expression was detectable in a dose dependent manner after 24h of IFN-γ stimulation only in HD conditions (Supplementary Fig. S4B). To determine that these results were through the inhibition of ER, we tested MCF7 cells with doxycycline (DOX)-induced expression of the *ESR1* Y537S activating mutation that engenders ligand-

independent ER activity. In response to IFN-γ stimulation, MHC-I expression in HD conditions was significantly lower in cells that expressed the Y537S mutation compared to the isogenic cells without the expression of the Y537S mutation and was comparable to the level of MHC-I detected in E2 treated conditions in the *ESR1*-WT and *ESR1*-Y537S mutant cells (Fig. 3F-3G). In contrast, treatment with the selective estrogen degrader, fulvestrant, or the novel ER degrader, ARV-471 (55), which have activity in the presence of the ER mutations, resulted in increased MHC-I expression (Supplementary Fig. S4C-4D). Furthermore, treatment with fulvestrant also resulted in enhanced MHC-I expression after IFN-γ stimulation in the presence of WT-ER (Fig. 3H-3I). Lastly, hormone deprivation did not influence IFN-γ-induced MHC-I expression in the MDA-MB-231 BC cells that do not express ER (Fig. 3J-3K). Since previous *in vivo* studies showed that T-cells produce a rapid single pulse of IFN-γ (56), we tested the MHC-I expression in response to a 15-minute pulse of IFN-γ**.** HD and fulvestrant treatment led to a robust increase in MHC-I expression in response to a pulse of IFN-γ that was comparable to continuous treatment with IFN-γ in HD conditions and fulvestrant treatment (the ratio of MHC-I levels between pulse and continuous IFN-γ after HD and fulvestrant was 1.18 and 1.27, respectively) (Fig. 3L). Since we also observed a strong increase in the expression of STING in primary ER+ breast tumors in the regions of immune and invasive epithelial cancer cells in response to ET, we tested STING levels in the MCF7 cells. In contrast to our findings in the tumor samples (Fig. 2I), we did not detect STING expression at baseline or after IFN-γ stimulation in HD or E2 conditions in MCF7 cells (Supplementary Fig. S4E). Thus, as opposed to the increase in MHC-I expression in response to ET and IFN-γ stimulation that is, at least in part, a cell intrinsic effect and observed in the BC cells in 2D culture, the effect of ET on STING expression is likely not cell intrinsic, but rather dependent on a more complex interplay between the cancer cells and the TME.

Although PD-L1 expression is immunosuppressive, it is a key target of ICIs and its expression is stimulated by IFN-γ. We therefore tested the impact of ET on IFN-γ induced PD-L1 levels. Like MHC-I expression, HD and fulvestrant treatment increased PD-L1 expression in response to IFN-γ (Fig. 3M-3P). Moreover, the effect of HD on the expression of PD-L1 was not seen in *ESR1*-Y537S mutant or ER-negative MDA-MB-231 cells (Supplementary Fig. S4F-4J). However, in contrast to the regulation of MHC-I, the increase in PD-L1 expression in response to HD and fulvestrant treatment was greater with continuous IFN-γ stimulation compared to the short pulse of IFN-γ (the ratio of PD-L1 levels between continuous and pulse IFN-γ stimulation in HD and fulvestrant treatment was 2.46 and 3.73, respectively) (Fig. 3Q), suggesting that ET may not have a significant impact on PD-L1 expression in physiological conditions. Likewise, in the PELOPS trial, we did not detect a significant change in PD-L1 levels after two or 24 weeks of ET.

ER inhibition enhances the response to IFN-γ stimulation

To gain mechanistic insights into how ER inhibition upregulates MHC-I levels, we performed RNA-seq in MCF7 cells in HD and E2 conditions with and without IFN-γ stimulation (Supplementary Table S8 and S9). We first looked at the genes that were differentially expressed in HD versus E2 growth conditions without IFN-γ stimulation (Fig. 4A). Hallmark pathway analysis showed enrichment of genes involved in the cell cycle, estrogen response, and mTOR1 signaling in E2 conditions (Fig. 4B). Interestingly, in HD conditions the upregulated genes were enriched in genes related to an immune response. Notably, NF-κB signaling was the most significantly enriched pathway (Fig. 4C). Unsupervised K-means clustering of the transcriptomes when evaluating the effects of IFN-γ in a time dependent manner, revealed three main gene groups that we designated as follows: E2-regulated, IFN-γ-early and IFN-γ-late genes (Fig. 4D and Supplementary Table S10). The E2-regulated group consists of genes that were upregulated in E2 conditions prior to IFN-γ stimulation and remained overexpressed

in E2 versus HD conditions after IFN-γ stimulation. Pathway analysis showed that these are E2 regulated genes (Fig. 4E). IFN-γ-early genes were overexpressed in HD conditions prior to IFN-γ stimulation and were further upregulated after IFN-γ stimulation with highest expression in HD condition after 6 hours of IFN-γ treatment. These genes were enriched in NF-κB signaling and IFN-γ signaling (Fig. 4F). The IFN-γ-late genes exhibited IFN-γ responsiveness in E2 and HD conditions with a higher degree of upregulation in HD conditions. However, prior to IFN-γ treatment, these genes had similar expression levels in HD and E2 conditions (Fig. 4G). Overall, there were more genes significantly upregulated and downregulated with IFN-γ in HD compared to E2 conditions at all time points (Log FC>1 adj p-value<0.01) (Supplementary Fig. S5A and Supplementary Tables S7 and S8). In keeping with the increase in the protein levels of MHC-I after hormone deprivation and the results of the DSP in the PELOPS cohort, higher transcript levels of B2M were seen in HD conditions. The increase in B2M was detected prior to IFN-γ stimulation (HD versus E2 condition)) and was enhanced after 6 and 12 hours of IFN-γ stimulation. Additionally, other genes of the MHC-I complex (HLA-A/ HLA-B/ HLA-C) and of the antigen presenting machinery (NLRC5, TAP1 and TAP2) were upregulated in HD conditions only after IFN-γ stimulation (Fig. 4H). Multiple transcripts directly related to the IFN signaling were also upregulated. Among these genes were the IFN-γ receptor heterodimers (IFNGR1 and IFNGR2) that had highest expression in HD conditions prior to IFN-γ stimulation, suggesting that in HD conditions, the cells are already poised to enhanced response to IFN-γ. In contrast, the expression of Interferon Regulatory Factors (IRF) genes that are downstream of the IFN-γ receptors was increased in HD conditions only after IFN-γ stimulation (Fig. 4H). Additionally, a gene set (CXCL9, CXCL10, IDO-1, HLA-DRA, and STAT1) that was shown to be predictive of response to ICI had increased expression after IFN-γ stimulation in HD conditions only (57).

To follow up on the increased expression of several chemokines/cytokines detected in HD conditions, we tested the levels of chemokines/cytokines secreted from MCF7 cells and confirmed an increase in CXCL10, a key chemoattractant of cytotoxic T cells, NK cells and Th1 cells (58), in HD conditions. Expression of the Y537S-ER completely suppressed the increased secretion of CXCL10 in HD condition, validating that this effect was through ER inhibition (Supplementary Fig. S5B). More broadly, the transcriptional differences between E2 and HD conditions after 24h of IFN-γ stimulation were diminished in the presence of the Y537S mutation (Supplementary Fig. S5C-5D). A direct comparison between WT versus Y537S mutant cells in HD conditions after IFN-γ stimulation revealed increased expression of B2M, IRF1, STAT1, CXCL9 and CXCL10 in the WT-ER cells. Pathway analysis showed that the genes upregulated in WT-ER cells are involved in IFN response pathways, whereas the genes upregulated in Y537S-ER mutant cells are enriched in ER-related pathways (Supplementary Fig. S5E-5G), further supporting the role of the inhibition of the ER transcriptional axis in the upregulation of IFN signaling.

To delineate the chromatin changes and identify the transcription factors involved in the disparate responses to IFN-γ in HD and E2 conditions, we studied chromatin accessibility applying the Assay for Transposase-Accessible Chromatin using sequencing (ATAC-seq). When we compared E2 versus HD conditions with and without IFN-γ stimulation, we identified 549 sites with gained chromatin accessibility in the E2 conditions (Fig. 4I). As expected, these sites were enriched in ERE and FOXA1 motifs (Supplementary Fig. S5H). There was a limited number of accessible sites gained in HD conditions (N=138). These were gained in HD conditions without and with IFN-γ stimulation and enriched in TEAD and AP1 motifs with a trend toward enrichment of RelA (NF-κB) motifs (Supplementary Fig. S5I). Intriguingly and in keeping with the RNA-seq data, when we tested the accessible sites gained after IFN-γ comparing HD and E2 conditions, we identified 2266 IFN-γ

stimulated sites unique to HD, 946 sites shared to both conditions, and only 294 sites unique to E2 conditions (Fig. 4J). As expected, all three groups of accessible sites were enriched in IRF motifs. There was also a trend toward enrichment of the RelA motif in the HD unique sites (Fig. 4K). In aggregate, our RNA-seq and ATAC-seq data indicate that ER+ BC cells are poised for an enhanced response to IFN-γ after ER blockade, and IFN-γ stimulation leads to an enhanced downstream response in HD conditions. Based on the RNA-seq pathway analysis and ATAC-seq motif analysis we hypothesized that these findings are due to enhanced NF-κB signaling, a signaling pathway involved in key physiological processes, including activation of the immune system, cell proliferation, and apoptosis (59) .

ER blockade augments RelA phosphorylation and transcriptional activity

To test our hypothesis that the enhanced transcription of IFN-γ related genes in HD condition in ER+ BC cells is through NF-κB signaling, we first assessed the levels of RelA (p65), the subunit of the canonical NF-κB complex that contains the transcriptional transactivation domain (TAD). While there were no significant changes in the level of total RelA in HD versus E2 conditions in MCF7 cells, phosphorylation of RelA at S536, a phosphorylation site within the TAD that promotes transactivation (60), was increased in HD conditions (Fig. 5A). In addition, RelB, a non-canonical subunit of NF-κB that also has a TAD and is a transcriptional target of RelA (61), was upregulated in HD conditions without and with IFN-γ stimulation at the transcript and protein level (Fig. 5A). Time dependent decrease and increase in S536 phosphorylation (p-RelA) with E2 exposure and HD, respectively, further substantiated the role of HD in p-RelA (Fig. 5B and Supplementary Fig. S6A). This effect was most likely a direct consequence of ER inhibition and not an effect secondary to the cell cycle arrest induced by E2 deprivation since treatment with the CDK4/6i palbociclib did not impact RelA

phosphorylation or RelB expression (Supplementary Fig. S6B). This is also indicative of the distinct mechanisms by which palbociclib (53) and ET augment antigen presentation.

To test the effect of ER blockade on RelA mediated transcription we performed RelA ChIP-seq. Remarkably, RelA binding was primarily detected in HD conditions (3775 RelA binding sites in HD conditions and only 360 binding sites in E2 conditions) (Fig. 5C). As expected, the RelA (NF-κB) motif was the most significantly enriched motif in the RelA binding sites (Supplementary Fig. S6C). The AP-1 motif was second most enriched motif, which is consistent with previous studies showing that NF-κB and AP-1 co-localize to form an inflammatory regulatory network (62). To test the direct transcriptional effects of RelA/NF-κB signaling in ER+ BC in HD conditions, we integrated the RelA ChIP-seq (binding sites in HD conditions) and RNA-seq (differential expression between HD and E2 conditions), employing the Binding and Expression Target Analysis (BETA) algorithm (41). This analysis revealed a significant association between the RelA binding sites and the genes upregulated (but not down regulated) in HD conditions compared to E2 conditions without IFN-γ stimulation (Fig. 5D). The BETA analysis also enabled us to identify the genes predicted to be direct RelA transcriptional targets in HD conditions (N=541 genes, see Methods). These genes, defined as the HD_RelA gene set (Supplementary Table S11), are involved in pathways of NF-κB signaling and IFN-γ response (Supplementary Fig. S6D). BETA analysis testing the genes that are direct targets of RelA in HD conditions after IFN-γ treatment also showed a significant association between RelA binding after IFN-γ treatment and genes upregulated in HD and IFN-γ stimulated conditions, but not the genes upregulated in E2 conditions (Supplementary Fig. S6E and Supplementary Table S12). Notably, RelA binding was detected in the promoter region of IFNGR2 in HD conditions (Supplementary Fig. S6F), which is consistent with the RNA-seq data in which we detected the upregulation of IFNGR2 in HD conditions (Fig. 3H) and suggests that IFNGR2 is a direct transcriptional target of RelA. Moreover,

RelA was the second top ranked transcription factor predicted to regulate IFNGR2 in publicly available ChIP-seq data sets (63), (Supplementary Fig. S6G). The clinical relevance of these findings is evidenced by the increased expression levels of the HD_RelA gene set after neoadjuvant treatment with an AI in primary ER+ BC biopsies obtained pre and post treatment (46) (Fig. 5E). In addition, the expression levels of the HD_RelA gene set inversely correlated with the ER levels in the TCGA cohort of primary ER+ BCs (Supplementary Fig. S6H).

To further validate that the transcriptional activity of RelA in ER+ BC cells is nearly restricted to HD conditions, we silenced RelA with CRISPR-Cas9 using two different single guide RNAs (gRNAs) (Supplementary Fig. S6I-6J). When assessing the transcriptional changes in a global manner, the effect of RelA silencing on transcription after 6h of IFN-γ treatment was seen only in HD conditions (Fig. 5F) or after fulvestrant treatment (Fig. 5G), with nearly no differentially expressed genes apart from RelA itself in E2 conditions (Fig. 5H). In addition, RelA silencing resulted mainly in the downregulation of gene expression, with the upregulation of only one gene in all three conditions (HD, fulvestrant, E2). These results corroborated our ChIP-seq and RNA-seq data, which showed that RelA-mediated chromatin binding and transcription is dependent on ER blockade, and the direct transcriptional effect is predominantly gene upregulation.

Although we detected transcriptional effects upon RelA silencing in HD conditions, these effects were relatively limited since only 53 genes significantly downregulated after 6h of IFN-γ treatment. This suggests that there may be other components of the NF-κB complex or other transcription factors that compensate for RelA loss. Nonetheless, RelA silencing resulted in the down regulation of IFN-γ target genes with key roles in antigen presentation that we identified as direct RelA transcriptional targets in ER+ BC cells, such as ICAM1 (64), HLA-A, TAP1, B2M, and CXCL10 (Fig. 5I-5J). The impact of RelA silencing on B2M was statistically significant but the absolute difference was limited, which is

consistent with the notion that other transcription factors, such as IRF-1, facilitate the upregulation of B2M in ER+ BC cells as in other cell types (65). Conversely, RelA was found to be essential for CXCL10 expression, as RelA silencing led to near complete loss of CXCL10 transcription.

Birinapant potentiates the antitumoral effect of ER blockade and enhances tumor immunogenicity

We next sought to investigate whether the effect of ET on NFKB can be leveraged for therapeutic purposes. To explore this, we examined the effects of combining a SMAC mimetic with ET in ER+ BC models. SMAC mimetics are a class of pro-apoptotic agents currently under clinical development that induce cIAP/XIAP protein degradation, leading to enhanced apoptosis. Additionally, they promote NF-κB signaling by stabilizing NFκB-inducing kinase (NIK) expression (66). Importantly, NF-κB exerts pro-survival effects partly through the induction of the cIAP proteins that interact with TRAF2 (67). Therefore, SMAC mimetics have the potential to enhance the immune effects while blocking the pro-survival effects of NF-κB. Moreover, a recent study showed that the SMAC mimetic, birinapant, increased response to ICIs in *in vivo* syngeneic models of melanoma (68).

We assessed the effect of birinapant on growth in ER+ BC cells. Single agent birinapant had a modest impact on cell growth as a single agent but enhanced the activity of fulvestrant (Fig. 6A). Remarkably, the combination of birinapant and fulvestrant was highly synergistic (Fig. 6B). Moreover, in an *in vivo* experiment of an ER+/HER2- patient derived xenograft (PDX), single agent birinapant significantly decreased tumor growth and the combination of birinapant and fulvestrant was superior with complete tumor regression in 4 of the 5 mice (Fig. 6C and Supplementary Fig. S7A-7D)

To investigate the mechanisms of the cell autonomous enhanced anti-tumor activity with the combination of birinapant and fulvestrant we performed RNAseq after 72h of treatment with vehicle, birinapant (100nM), fulvestrant (10nM) and the combination of these two drugs. Gene set enrichment analysis (GSEA) of the transcriptomic changes after treatment with birinapant, fulvestrant and the combination showed upregulation of the apoptosis pathway (Supplementary Table S13), inhibition of ER signaling and the cell cycle (Fig. 6D). These convergent transcriptional effects may explain the synergy we observed. Pathway analysis also revealed an increase in NF-κB signaling and IFN-γ and IFN-α response with each of these drugs as single agents as well as the combination of these two drugs.

When comparing the genes induced by IFN-γ in the presence of fulvestrant, birinapant, and the combination (Log 2FC>1, q-value <0.01) we detected 293 shared genes and 167 genes that were uniquely upregulated with the combination (Supplementary Fig. S8A). Furthermore, K-means analysis identified three gene sets, including: 1. A gene set (defined as immune) that increased after IFN-γ treatment with vehicle control and was further upregulated with the combination of fulvestrant and birinapant (N=407 genes). This gene set was enriched in genes involved in IFN-γ response, IFN-α response, allograft rejection, complement, and TNF-α signaling via NF-κB . 2. A gene set we termed inflammatory (N=219 genes) that increased after IFN-γ stimulation in the presence of fulvestrant and the combination of fulvestrant and birinapant. 3. The third gene set defined as ER (N= 317 genes) was downregulated after treatment with fulvestrant and the combination of fulvestrant and birinapant (Supplementary Fig. S8B). Looking at specific genes, we identified key members of the antigen presenting machinery, including B2M, HLA-A/B, TAP1, TAP2, NLRC5, and the IFN-γ-JAK-STAT pathway (IFNG1, IFNG2, IRF1) among the genes that had enhanced expression with the combination of birinapant and fulvestrant compared to vehicle control or each drug alone (Fig. 7A).

At the protein level, birinapant enhanced MHC-I and PD-L1 expression in a dose-dependent manner in HD and IFN-γ stimulated conditions but not in E2 treated conditions (Fig. 7B-7C). Likewise, increasing concentrations of birinapant in combination with fulvestrant enhanced MHC-I and PD-L1 expression (Fig. 7D-7E). Detailed protein analysis of the NF-κB complex showed that birinapant alone or in combination with fulvestrant did not impact RelA, p105, and p50 (NFκB1) levels (Fig. 7F). In contrast, birinapant in combination with fulvestrant increased RelA S536 phosphorylation prior to and after IFN-γ stimulation. After IFN-γ stimulation, the combination of birinapant and fulvestrant increased RelB levels. In addition, birinapant alone and in combination with fulvestrant increased the processing of the inactive p100 NFκB2 protein to p52, the active NFκB2 protein, prior to and after IFN-γ stimulation, This in keeping with the role of SMAC mimetics in stabilization of NIK and subsequent phosphorylation and activation of IKKα (Fig. 7F) (66). Phosphorylation of STAT1 (p-STAT1) and IRF-1, both downstream to IFNG2, a RelA transcriptional target gene, was detected only after IFN-γ stimulation and had increased levels after treatment with fulvestrant or the combination of fulvestrant and birinapant (Fig. 7F). Similarly, in T47D cells, we observed an increase in p-RelA after fulvestrant treatment, which was enhanced with the combination of fulvestrant and birinapant (Supplementary Fig. S8C). Likewise, RelB, MHC-I and IRF1 expression increased in T47D cells after treatment with the combination of fulvestrant and birinapant in IFN-γ stimulated conditions (Supplementary Fig. S8C).

Profiling of the secretome (N=105) in the culture medium of MCF7 cells treated with fulvestrant, birinapant, and the combination revealed that the combination of fulvestrant and birinapant augmented CXCL10 and CXCL9 secretion, supporting the RNAseq results (Supplementary Fig. S8D-8E). To determine the functional consequences of this finding, we performed a T-cell 3D migration test (Supplementary Fig. S8F) and detected increased T-cell migration towards MCF7 tumor spheroids in the presence of birinapant, which was significantly increased when fulvestrant was combined with

birinapant (Fig. 7G-7H). To test the effects of fulvestrant and birinapant on the anti-tumor activity of T-cells mediated by specific recognition of an MHC-I-peptide complex by the specific T-cell receptor in ER+ BC, we developed a co-culturing assay. We stably expressed NY-ESO-1 in MCF7 cells, which have an HLA-A*0201 genotype, and generated CD8+ T-cells stably expressing a T-cell receptor (TCR) that specifically recognizes the complex of the NY-ESO-1 peptide antigen bound to MHC-I with an HLA-A*0201 allotype. After co-culturing the NY-ESO-1-MCF7 cells and the activated engineered T-cells we observed increased T-cell mediated cytotoxicity with evidence of granzyme B secretion from the T-cells after birinapant treatment and an enhanced effect with fulvestrant plus birinapant (Fig. 7I-7J). In contrast, after co-culturing NY-ESO-1-MCF7 cells with CD8+ T-cells without the expression of the engineered TCR, there was no evidence of granzyme B secretion or T cell-mediated cytotoxicity (Supplementary Fig. S8G-8H), validating the role of specific antigen peptide-TCR interaction in the observed cytotoxicity. In aggregate, these results provide a two-fold rationale for the combination of ET and birinapant, including: (i) Cell autonomous synergistic tumor regression, and (ii) Enhanced immune-mediated cancer cell cytotoxicity through increased migration of T-cells, and tumor infiltration with cytotoxic T-cells along with increased antigen presentation and T-cell recognition of ER+ cancer cells.

Discussion

In clinical trials the activity ICIs in HR+ BC was shown to be limited. Furthermore, there is a paucity of information about the effects of ET on the TME and tumor immunogenicity. We performed a spatial proteomics analysis in primary HR+ BCs before and after ET alone and in combination with palbociclib to evaluate key immune related proteins that are determinants of tumor immunogenicity. The most significant effects of ET alone and in combination with palbociclib were increases in STING and B2-microglobulin in both immune and ICECs regions. Albeit the levels of STING and B2-

microglobulin remained higher in the immune regions compared to the ICECs. In addition, in the ICECs regions, there was an increase in several immune check points, such as TIM-3, B7-H3, and CTLA-4. While the predictive or prognostic significance of these findings is unknown, these findings provide compelling evidence for the role of ET in shaping the TME in HR+ BC. Moreover, our results indicate that ET amy improve outcomes when combined with immune therapies in ER+ BC. Furthermore, our results suggest that the CTLA4-inhibitor ipilimumab, or inhibitors of B7-H3 or TIM-3 that are currently in clinical development (69, 70), may be more effective in combination with ET compared to PD-1 or PD-L1 inhibitors in HR+ BC.

We investigated the mechanism by which ET increases the expression of MHC-I in invasive cancer cells. Through these studies we found that ER blockade is required for NF-κB signaling in ER+ BC cells, which in turn mediates the expression of B2M in addition to key cytokines such as CXCL10. The activation of NF-κB also enhances the activation of the IFNGR2-JAK-STAT pathway, supporting the interaction between the NF-κB and IRF transcriptional networks (71). These results are consistent with and provide a mechanism to the inverse correlation between ER signaling and antigen presentation that was seen in the recent analysis of a clinical trial of chemotherapy in combination with pembrolizumab in metastatic HR+ BC (13). These results are also in line with studies that demonstrated a cross talk between ER and NF-κB. Previous studies showed that ER inhibits NF-κB mediated transcription in reporter gene assays, and a direct interaction between ER and NF-κB was detected in models of recombinant ER (72). We performed a genome-wide study and demonstrated that endogenous RelA binding is diminished when ER is active in ER+ BC cells. Furthermore, we delineated the direct transcriptional consequences of NF-κB transcriptional activity after ER inhibition and provide evidence for the clinical relevance of these findings. We also demonstrated that ER inhibition upregulated RelA phosphorylation at a transactivation site. ER-mediated suppression of RelA phosphorylation was reported previously and attributed, at least in part, to the upregulation of the long non-coding RNA

LINC00472 induced by ER (73). However, other potential mechanisms may contribute to the effect of ER on RelA phosphorylation. Overall, the mechanism by which ER facilitates RelA phosphorylation and how RelA phosphorylation impacts RelA chromatin binding in ER+ BC cells warrant additional investigation.

We showed that after ER blockade, ER+ BC cells are poised to an enhanced response to IFN-γ through NF-κB signaling. We observed that key genes of the antigen presentation machinery and cytokines, are upregulated after ET prior to IFN-γ stimulation. Given these findings, we investigated if enhancing NF-κB signaling could elicit an increased anti-tumor immune response in ER+ BC by testing the effects of the SMAC mimetic birinapant. Previous studies showed that NF-κB signaling plays a role in acquired resistance to ET, raising concerns about the therapeutic potential of enhancing NF-κB signaling (74). However, SMAC mimetics have dual effects; stabilization of NIK to promote NF-KB mediated immune signaling and induction of cIAP/XIAP protein degradation, leading to enhanced apoptosis. Moreover, NF-κB's pro-survival effects are partly mediated through the induction of the cIAP proteins (67). Consequently, as we demonstrated, the addition of the SMAC mimetic birinapant to ET, increased the expression of NF-κB immune target genes leading to the migration of T-cells towards ER+ BC cells and MHC-I specific T cell-mediated cell death in ER+ BC cells, while also increasing tumor regression in a cell autonomous manner. Taken together, these results coupled with the safety profile of SMAC-mimetics (75, 76), provide a rationale for the ET plus SMAC mimetics in combination with immunotherapy in HR+ BC.

References

1. Wolchok JD, Kluger H, Callahan MK, Postow MA, Rizvi NA, Lesokhin AM, et al. Nivolumab plus ipilimumab in advanced melanoma. N Engl J Med. 2013;369(2):122-33.
2. Korde LA, Somerfield MR, Hershman DL, Neoadjuvant Chemotherapy ET, Targeted Therapy for Breast Cancer Guideline Expert P. Use of Immune Checkpoint Inhibitor Pembrolizumab in the Treatment of High-Risk, Early-Stage Triple-Negative Breast Cancer: ASCO Guideline Rapid Recommendation Update. J Clin Oncol. 2022:JCO2200503.
3. Cortes J, Cescon DW, Rugo HS, Nowecki Z, Im SA, Yusof MM, et al. Pembrolizumab plus chemotherapy versus placebo plus chemotherapy for previously untreated locally recurrent inoperable or metastatic triple-negative breast cancer (KEYNOTE-355): a randomised, placebo-controlled, double-blind, phase 3 clinical trial. Lancet. 2020;396(10265):1817-28.
4. Zacharakis N, Chinnasamy H, Black M, Xu H, Lu YC, Zheng Z, et al. Immune recognition of somatic mutations leading to complete durable regression in metastatic breast cancer. Nat Med. 2018;24(6):724-30.
5. Rugo HS, Delord JP, Im SA, Ott PA, Piha-Paul SA, Bedard PL, et al. Safety and Antitumor Activity of Pembrolizumab in Patients with Estrogen Receptor-Positive/Human Epidermal Growth Factor Receptor 2-Negative Advanced Breast Cancer. Clin Cancer Res. 2018;24(12):2804-11.
6. Nanda R, Liu MC, Yau C, Shatsky R, Pusztai L, Wallace A, et al. Effect of Pembrolizumab Plus Neoadjuvant Chemotherapy on Pathologic Complete Response in Women With Early-Stage Breast Cancer: An Analysis of the Ongoing Phase 2 Adaptively Randomized I-SPY2 Trial. JAMA Oncol. 2020;6(5):676-84.
7. Stanton SE, Adams S, Disis ML. Variation in the Incidence and Magnitude of Tumor-Infiltrating Lymphocytes in Breast Cancer Subtypes: A Systematic Review. JAMA Oncol. 2016;2(10):1354-60.
8. Voutsadakis IA. High Tumor Mutation Burden and Other Immunotherapy Response Predictors in Breast Cancers: Associations and Therapeutic Opportunities. Target Oncol. 2020;15(1):127-38.
9. Van Allen EM, Miao D, Schilling B, Shukla SA, Blank C, Zimmer L, et al. Genomic correlates of response to CTLA-4 blockade in metastatic melanoma. Science. 2015;350(6257):207-11.
10. Sade-Feldman M, Jiao YJ, Chen JH, Rooney MS, Barzily-Rokni M, Eliane JP, et al. Resistance to checkpoint blockade therapy through inactivation of antigen presentation. Nat Commun. 2017;8(1):1136.
11. Gettinger S, Choi J, Hastings K, Truini A, Datar I, Sowell R, et al. Impaired HLA Class I Antigen Processing and Presentation as a Mechanism of Acquired Resistance to Immune Checkpoint Inhibitors in Lung Cancer. Cancer Discov. 2017;7(12):1420-35.
12. Lee HJ, Song IH, Park IA, Heo SH, Kim YA, Ahn JH, et al. Differential expression of major histocompatibility complex class I in subtypes of breast cancer is associated with estrogen receptor and interferon signaling. Oncotarget. 2016;7(21):30119-32.
13. Keenan TE, Guerriero JL, Barroso-Sousa R, Li T, O'Meara T, Giobbie-Hurder A, et al. Molecular correlates of response to eribulin and pembrolizumab in hormone receptor-positive metastatic breast cancer. Nat Commun. 2021;12(1):5563.
14. Bengtsson AK, Ryan EJ, Giordano D, Magaletti DM, Clark EA. 17beta-estradiol (E2) modulates cytokine and chemokine expression in human monocyte-derived dendritic cells. Blood. 2004;104(5):1404-10.
15. Cunningham M, Gilkeson G. Estrogen receptors in immunity and autoimmunity. Clin Rev Allergy Immunol. 2011;40(1):66-73.

16. Svoronos N, Perales-Puchalt A, Allegrezza MJ, Rutkowski MR, Payne KK, Tesone AJ, et al. Tumor Cell-Independent Estrogen Signaling Drives Disease Progression through Mobilization of Myeloid-Derived Suppressor Cells. Cancer Discov. 2017;7(1):72-85.
17. Chakraborty B, Byemerwa J, Shepherd J, Haines CN, Baldi R, Gong W, et al. Inhibition of estrogen signaling in myeloid cells increases tumor immunity in melanoma. J Clin Invest. 2021;131(23).
18. Merritt CR, Ong GT, Church SE, Barker K, Danaher P, Geiss G, et al. Multiplex digital spatial profiling of proteins and RNA in fixed tissue. Nat Biotechnol. 2020;38(5):586-99.
19. Bates D, Mächler M, Bolker B, Walker S. Fitting Linear Mixed-Effects Models Using lme4. Journal of Statistical Software. 2015;67(1):1 - 48.
20. Kuznetsova A, Brockhoff PB, Christensen RHB. lmerTest Package: Tests in Linear Mixed Effects Models. Journal of Statistical Software. 2017;82(13):1 - 26.
21. Li X, Gruosso T, Zuo D, Omeroglu A, Meterissian S, Guiot MC, et al. Infiltration of CD8(+) T cells into tumor cell clusters in triple-negative breast cancer. Proc Natl Acad Sci U S A. 2019;116(9):3678-87.
22. Salgado R, Denkert C, Demaria S, Sirtaine N, Klauschen F, Pruneri G, et al. The evaluation of tumor-infiltrating lymphocytes (TILs) in breast cancer: recommendations by an International TILs Working Group 2014. Ann Oncol. 2015;26(2):259-71.
23. Jeselsohn R, Bergholz JS, Pun M, Cornwell M, Liu W, Nardone A, et al. Allele-Specific Chromatin Recruitment and Therapeutic Vulnerabilities of ESR1 Activating Mutations. Cancer Cell. 2018;33(2):173-86 e5.
24. Bagati A, Kumar S, Jiang P, Pyrdol J, Zou AE, Godicelj A, et al. Integrin alphavbeta6-TGFbeta-SOX4 Pathway Drives Immune Evasion in Triple-Negative Breast Cancer. Cancer Cell. 2021;39(1):54-67 e9.
25. Chi D, Singhal H, Li L, Xiao T, Liu W, Pun M, et al. Estrogen receptor signaling is reprogrammed during breast tumorigenesis. Proc Natl Acad Sci U S A. 2019;116(23):11437-43.
26. Li H, Durbin R. Fast and accurate long-read alignment with Burrows-Wheeler transform. Bioinformatics. 2010;26(5):589-95.
27. Zhang Y, Liu T, Meyer CA, Eeckhoute J, Johnson DS, Bernstein BE, et al. Model-based analysis of ChIP-Seq (MACS). Genome Biol. 2008;9(9):R137.
28. Feng J, Liu T, Qin B, Zhang Y, Liu XS. Identifying ChIP-seq enrichment using MACS. Nat Protoc. 2012;7(9):1728-40.
29. Neph S, Kuehn MS, Reynolds AP, Haugen E, Thurman RE, Johnson AK, et al. BEDOPS: high-performance genomic feature operations. Bioinformatics. 2012;28(14):1919-20.
30. Qiu X, Feit AS, Feiglin A, Xie Y, Kesten N, Taing L, et al. CoBRA: Containerized Bioinformatics Workflow for Reproducible ChIP/ATAC-seq Analysis. Genomics Proteomics Bioinformatics. 2021.
31. Buenrostro JD, Giresi PG, Zaba LC, Chang HY, Greenleaf WJ. Transposition of native chromatin for fast and sensitive epigenomic profiling of open chromatin, DNA-binding proteins and nucleosome position. Nat Methods. 2013;10(12):1213-8.
32. Buenrostro JD, Wu B, Chang HY, Greenleaf WJ. ATAC-seq: A Method for Assaying Chromatin Accessibility Genome-Wide. Curr Protoc Mol Biol. 2015;109:21 9 1- 9 9.
33. Li H, Durbin R. Fast and accurate short read alignment with Burrows-Wheeler transform. Bioinformatics. 2009;25(14):1754-60.
34. Love MI, Huber W, Anders S. Moderated estimation of fold change and dispersion for RNA-seq data with DESeq2. Genome Biol. 2014;15(12):550.

35. Cornwell M, Vangala M, Taing L, Herbert Z, Koster J, Li B, et al. VIPER: Visualization Pipeline for RNA-seq, a Snakemake workflow for efficient and complete RNA-seq analysis. BMC Bioinformatics. 2018;19(1):135.
36. Kuang Y, Siddiqui B, Hu J, Pun M, Cornwell M, Buchwalter G, et al. Unraveling the clinicopathological features driving the emergence of ESR1 mutations in metastatic breast cancer. NPJ Breast Cancer. 2018;4:22.
37. Trapnell C, Williams BA, Pertea G, Mortazavi A, Kwan G, van Baren MJ, et al. Transcript assembly and quantification by RNA-Seq reveals unannotated transcripts and isoform switching during cell differentiation. Nat Biotechnol. 2010;28(5):511-5.
38. Wang L, Wang S, Li W. RSeQC: quality control of RNA-seq experiments. Bioinformatics. 2012;28(16):2184-5.
39. Subramanian A, Tamayo P, Mootha VK, Mukherjee S, Ebert BL, Gillette MA, et al. Gene set enrichment analysis: a knowledge-based approach for interpreting genome-wide expression profiles. Proc Natl Acad Sci U S A. 2005;102(43):15545-50.
40. Hanzelmann S, Castelo R, Guinney J. GSVA: gene set variation analysis for microarray and RNA-seq data. BMC Bioinformatics. 2013;14:7.
41. Wang S, Sun H, Ma J, Zang C, Wang C, Wang J, et al. Target analysis by integration of transcriptome and ChIP-seq data with BETA. Nat Protoc. 2013;8(12):2502-15.
42. Guillen KP, Fujita M, Butterfield AJ, Scherer SD, Bailey MH, Chu Z, et al. A human breast cancer-derived xenograft and organoid platform for drug discovery and precision oncology. Nat Cancer. 2022;3(2):232-50.
43. Yadav B, Wennerberg K, Aittokallio T, Tang J. Searching for Drug Synergy in Complex Dose-Response Landscapes Using an Interaction Potency Model. Comput Struct Biotechnol J. 2015;13:504-13.
44. Aref AR, Campisi M, Ivanova E, Portell A, Larios D, Piel BP, et al. 3D microfluidic ex vivo culture of organotypic tumor spheroids to model immune checkpoint blockade. Lab Chip. 2018;18(20):3129-43.
45. Cancer Genome Atlas N. Comprehensive molecular portraits of human breast tumours. Nature. 2012;490(7418):61-70.
46. Miller CA, Gindin Y, Lu C, Griffith OL, Griffith M, Shen D, et al. Aromatase inhibition remodels the clonal architecture of estrogen-receptor-positive breast cancers. Nat Commun. 2016;7:12498.
47. Dowsett M, Smith IE, Ebbs SR, Dixon JM, Skene A, Griffith C, et al. Short-term changes in Ki-67 during neoadjuvant treatment of primary breast cancer with anastrozole or tamoxifen alone or combined correlate with recurrence-free survival. Clin Cancer Res. 2005;11(2 Pt 2):951s-8s.
48. Wagner J, Rapsomaniki MA, Chevrier S, Anzeneder T, Langwieder C, Dykgers A, et al. A Single-Cell Atlas of the Tumor and Immune Ecosystem of Human Breast Cancer. Cell. 2019;177(5):1330-45 e18.
49. Pardoll DM, Topalian SL. The role of CD4+ T cell responses in antitumor immunity. Curr Opin Immunol. 1998;10(5):588-94.
50. Dudley ME, Wunderlich JR, Robbins PF, Yang JC, Hwu P, Schwartzentruber DJ, et al. Cancer regression and autoimmunity in patients after clonal repopulation with antitumor lymphocytes. Science. 2002;298(5594):850-4.
51. Zhou P, Shaffer DR, Alvarez Arias DA, Nakazaki Y, Pos W, Torres AJ, et al. In vivo discovery of immunotherapy targets in the tumour microenvironment. Nature. 2014;506(7486):52-7.
52. Wakamatsu E, Mathis D, Benoist C. Convergent and divergent effects of costimulatory molecules in conventional and regulatory CD4+ T cells. Proc Natl Acad Sci U S A. 2013;110(3):1023-8.

53. Goel S, DeCristo MJ, Watt AC, BrinJones H, Sceneay J, Li BB, et al. CDK4/6 inhibition triggers anti-tumour immunity. Nature. 2017;548(7668):471-5.
54. Deng J, Wang ES, Jenkins RW, Li S, Dries R, Yates K, et al. CDK4/6 Inhibition Augments Antitumor Immunity by Enhancing T-cell Activation. Cancer Discov. 2018;8(2):216-33.
55. Lin X, Xiang H, Luo G. Targeting estrogen receptor alpha for degradation with PROTACs: A promising approach to overcome endocrine resistance. Eur J Med Chem. 2020;206:112689.
56. Hosking MP, Flynn CT, Whitton JL. Antigen-specific naive CD8+ T cells produce a single pulse of IFN-gamma in vivo within hours of infection, but without antiviral effect. J Immunol. 2014;193(4):1873-85.
57. Ayers M, Lunceford J, Nebozhyn M, Murphy E, Loboda A, Kaufman DR, et al. IFN-gamma-related mRNA profile predicts clinical response to PD-1 blockade. J Clin Invest. 2017;127(8):2930-40.
58. Schoenborn JR, Wilson CB. Regulation of interferon-gamma during innate and adaptive immune responses. Adv Immunol. 2007;96:41-101.
59. Zhang Q, Lenardo MJ, Baltimore D. 30 Years of NF-kappaB: A Blossoming of Relevance to Human Pathobiology. Cell. 2017;168(1-2):37-57.
60. Chen LF, Williams SA, Mu Y, Nakano H, Duerr JM, Buckbinder L, et al. NF-kappaB RelA phosphorylation regulates RelA acetylation. Mol Cell Biol. 2005;25(18):7966-75.
61. Bren GD, Solan NJ, Miyoshi H, Pennington KN, Pobst LJ, Paya CV. Transcription of the RelB gene is regulated by NF-kappaB. Oncogene. 2001;20(53):7722-33.
62. Ji Z, He L, Regev A, Struhl K. Inflammatory regulatory network mediated by the joint action of NF-kB, STAT3, and AP-1 factors is involved in many human cancers. Proc Natl Acad Sci U S A. 2019;116(19):9453-62.
63. Zheng R, Wan C, Mei S, Qin Q, Wu Q, Sun H, et al. Cistrome Data Browser: expanded datasets and new tools for gene regulatory analysis. Nucleic Acids Res. 2019;47(D1):D729-D35.
64. Lebedeva T, Dustin ML, Sykulev Y. ICAM-1 co-stimulates target cells to facilitate antigen presentation. Curr Opin Immunol. 2005;17(3):251-8.
65. Taniguchi T, Ogasawara K, Takaoka A, Tanaka N. IRF family of transcription factors as regulators of host defense. Annu Rev Immunol. 2001;19:623-55.
66. Morrish E, Brumatti G, Silke J. Future Therapeutic Directions for Smac-Mimetics. Cells. 2020;9(2).
67. Vaux DL, Silke J. IAPs, RINGs and ubiquitylation. Nat Rev Mol Cell Biol. 2005;6(4):287-97.
68. Gu SS, Zhang W, Wang X, Jiang P, Traugh N, Li Z, et al. Therapeutically Increasing MHC-I Expression Potentiates Immune Checkpoint Blockade. Cancer Discov. 2021;11(6):1524-41.
69. Gomes de Morais AL, Cerda S, de Miguel M. New Checkpoint Inhibitors on the Road: Targeting TIM-3 in Solid Tumors. Curr Oncol Rep. 2022;24(5):651-8.
70. Lee JB, Ha SJ, Kim HR. Clinical Insights Into Novel Immune Checkpoint Inhibitors. Front Pharmacol. 2021;12:681320.
71. Iwanaszko M, Kimmel M. NF-kappaB and IRF pathways: cross-regulation on target genes promoter level. BMC Genomics. 2015;16:307.
72. Kalaitzidis D, Gilmore TD. Transcription factor cross-talk: the estrogen receptor and NF-kappaB. Trends Endocrinol Metab. 2005;16(2):46-52.
73. Wang Z, Katsaros D, Biglia N, Shen Y, Loo L, Yu X, et al. ERalpha upregulates the expression of long non-coding RNA LINC00472 which suppresses the phosphorylation of NF-kappaB in breast cancer. Breast Cancer Res Treat. 2019;175(2):353-68.
74. Nehra R, Riggins RB, Shajahan AN, Zwart A, Crawford AC, Clarke R. BCL2 and CASP8 regulation by NF-kappaB differentially affect mitochondrial function and cell fate in antiestrogen-sensitive and -resistant breast cancer cells. FASEB J. 2010;24(6):2040-55.

75. Infante JR, Dees EC, Olszanski AJ, Dhuria SV, Sen S, Cameron S, et al. Phase I dose-escalation study of LCL161, an oral inhibitor of apoptosis proteins inhibitor, in patients with advanced solid tumors. J Clin Oncol. 2014;32(28):3103-10.
76. Amaravadi RK, Schilder RJ, Martin LP, Levin M, Graham MA, Weng DE, et al. A Phase I Study of the SMAC-Mimetic Birinapant in Adults with Refractory Solid Tumors or Lymphoma. Mol Cancer Ther. 2015;14(11):2569-75.

Figure Legends

Figure 1. Digital spatial analysis. (A) Schema of the Endocrine Therapy for Lobular Breast Cancer Preoperative Study (PELOPS, NCT02764541). Numbers (N) represent the number of tissue samples included in the digital spatial profiling. **(B)** Representative images of immunofluorescence staining for the regions of interest. CD45(cyan), E-cadherin(red) and pan-cytokeratin (green). The magnified panels represent two regions of interest (ROI); immune (#6) and invasive epithelial cells (#2) **(C-E**) Volcano plot of log2 fold changes and adjusted p-values of tests for differential protein expression comparing pre and post 24 weeks of endocrine treatment (2 weeks versus surgical) within invasive epithelial cellular regions **[C]** and corresponding individual average patient trajectories for Beta-2-Microglobulin **[D]** and progesterone receptor (PR) **[E]**. **(F-H)** Volcano plot of log2 fold changes and adjusted p-values of tests for differential protein expression comparing pre and post 24 weeks of endocrine treatment (2 weeks versus surgical) within immune regions **[F]** and corresponding individual mean patient trajectories for Beta-2-Microglobulin **[G]** and CD4 **[H]**. Horizontal dotted line denotes a 5% FDR threshold.

Figure 2. Endocrine treatment shapes tumor immune microenvironment in primary hormone receptor positive breast cancer. (**A-F)** Digital spatial profiling proteomic levels (log2 expression levels) of immune cell surface markers ranking from highest to lowest expression. **[A]** Baseline levels within the immune regions in tumors from patients that received endocrine therapy ($F(11, 312) = 57.1$, p-value < 2e-16, one-way ANOVA). **[B]** Protein expression levels within the immune regions after 2 weeks of endocrine treatment ($F(11, 276) = 41.7$, p-value < 2e-16, one-way ANOVA). **[C]** Protein expression levels within the immune regions after 24 weeks of endocrine treatment at the time of surgery ($F(11, 1212) = 305.2$, p-value < 2e-16, one-way ANOVA) **[D]** Baseline levels within the

invasive epithelial cell regions in tumors from patients that received endocrine therapy ($F(11, 732) = 126.3$, $p < 2e\text{-}16$, one-way ANOVA). **[E]** Protein expression levels within the invasive epithelial regions after 2 weeks of endocrine treatment (p-value < 2e-16, one-way ANOVA). **[F]** Protein expression levels within the invasive epithelial cell regions after 24 weeks of endocrine treatment at the time of surgery (p-value < 2e-16, one-way ANOVA). Boxplots show median, 25th, and 75th percentiles as boxes, the minimum of the 75th percentile + 1.5 * IQR and the maximum observation as the upper whisker and the maximum of the 25th percentile - 1.5 * IQR and the minimum observation as the lower whisker. **(G)** Trajectory plot of TIL fractions between baseline and 2 weeks. P-val denotes P-value (paired Wilcoxon signed-rank test with continuity correction). **(H)** Trajectory plot of TIL fractions between 2 weeks and surgery for all patients given endocrine treatment that have TIL observations at all three timepoints. Each trajectory corresponds to a single patient. P-val denotes P-value (paired Wilcoxon signed-rank test with continuity correction). **(I)** Gene Set Variation Analysis (GSVA) of the T-cell accumulation gene set in primary ER+ breast cancer biopsies from pre and post-neoadjuvant AI treatment**. (J)** Enrichment plot of the top ranked gene set (Estrogen response) enriched in the ESR1 highest (4^{th} quartile) versus ESR1 lowest (1^{st} quartile) estrogen receptor positive breast cancer samples from the TCGA cohort. (**K-M)** GSVA of RNA-seq from the estrogen receptor positive breast cancer samples from The Cancer Genome Atlas (TCGA) divided to quartiles based on ESR1 mRNA levels testing the enrichment score (Y-axis) for signatures of immune checkpoint blockade (ICB) resistance **[K]** T-regulatory (T-reg) accumulation **[L]** and cytotoxic T-cell accumulation **[M]**. Comparison between the quartiles was done with a t-test. N indicates the number of patients included in the corresponding analysis.

Figure 3. Estradiol modulates response to IFNg stimulation. **(A)** Histogram of MHC-I levels assessed by flow cytometry following 3 days of estradiol (E2) stimulation or hormone deprivation (HD)

in the presence or absence of IFNg (10 ng/mL) for the last 24h in MCF7 cells. **(B)** Quantification of median fluorescence intensity (MFI) of MHC-I from **[A]**. Values are normalized to E2 stimulation with vehicle control (No IFNg) cells. **(C-E)** MHC-I levels assessed by flow cytometry following 3 days of estradiol (E2) stimulation or hormone deprivation (HD) in the presence or absence of IFNg (10ug/mL) for the last 24h in ER+ T47D cells **[C]**, CAMA1 cells **[D]** and ZR75.1 **[E]**. Histograms **(F)** and MFI quantification **(G)** of MHC-I levels following 3 days of E2 stimulation (E2) or hormone deprivation (HD) in the presence or absence of IFNg (10 ng/mL) for the last 24h in MCF7 cells expressing the ESR1 Y537S mutation induced by doxycycline (DOX) treatment cells. Two-way ANOVA). **(H)** Histogram of MHC-I levels assessed by flow cytometry following 3 days of vehicle or fulvestrant (10 nM) treatment in the presence or absence of IFNg (10 ng/mL) for the last 24h in MCF7 cells. (**I**) MFI quantification of MHC-I from **[H].** Values are normalized to vehicle control (No IFNg) cells (*p< 0.05; Error bars are mean ± s.d of at least 2 replicates. Paired t-test). **(J)** Histogram of MHC-I levels assessed by flow cytometry following 3 days of E2 stimulation or HD in the presence or absence of IFNg (10 ng/mL) for the last 24h in ER negative MDA-MB-231 cells. **(K)** MFI quantification of MHC-I from **[J]** values are normalized to E2 stimulation (No IFNg) cells. **(L)** MFI quantification of MHC-I levels assessed by flow cytometry of cells grown in HD, E2 conditions or treated with fulvestrant or DMSO for 72h in the absence of IFNg (No IFNg) or with a 15-minute treatment of IFNg (10 ng/mL) 24h prior flow analysis (Pulse) or for the last 24h (Continuous=cont) prior to flow cytometry analysis. **(M)** PDL1 levels assessed by flow cytometry following 3 days of E2 stimulation or HD in the presence or absence of IFNg (10 ng/mL) x24h in MCF7 cells. **(N)** MFI quantification of MHC-I from **[M]**. **(O**) PD-L1 levels assessed by flow cytometry following 3 days of vehicle or fulvestrant (10 nM) treatment in the presence or absence of IFNg (10 ng/mL) x24h in MCF7 cells. (**P**) MFI quantification of MHC-I from **[O]. (Q)** MFI quantification of PDL1 levels assessed by flow cytometry after treatment for 72h in the absence of IFNg (No IFNg), with a 15-minute treatment of IFNg (10 ng/mL) 24h prior to flow

cytometry analysis (Pulse) or for the last 24h (Continuous=cont) prior to flow cytometry analysis. Statistics for the panel, if not mentioned differently, are: (***p< 0.001; n.s. not significant. Error bars are mean ± s.d of at least 2 replicates. Two-way ANOVA).

Figure 4. E**strogen deprivation upregulates IFNg response through NFKB signaling**. **(A)** RNA-seq analysis of MCF-7 cells grown in hormone deprived (HD) conditions or in the presence of estradiol (E2) for three days. The volcano plot shows genes differently expressed between HD and estradiol treated conditions (log2fFC>1, p_adj<0.01). Number on the top shows the total number of genes differentially expressed for each condition. **(B)** Gene set enrichment analysis of upregulated pathways in estradiol stimulated cells. **(C)** Gene set enrichment analysis of upregulated pathways in the HD condition. **(D)** 3 cluster K-means plot of genes without and with IFNg stimulation at different time points in cells grown in HD or E2 conditions with and without estradiol for 3 days. Hallmark pathway analysis of **(E)** "E2 induced" genes**, (F)** "IFNg early", and **(G)** "IFNg late". (FDR<0.05) **(H)** Supervised heat map of the expression of IFNg and antigen presentation related genes in estradiol (E2) treated and HD condition without and with IFNg treatment. **(I-J)** ATAC-seq that was performed in MCF7 cells grown in the presence or absence of E2 for 48 hours and followed by +/- IFNg 10 ng/mL stimulation for 24 hours. [**I**] Tornado plots of chromatin accessibility sites based on ATAC-seq showing accessible sites significantly different between E2 and HD conditions showing IFNg treated or no IFNg treated conditions. [**J**] Tornado plots showing the chromatin sites accessible induced by IFNg stimulation in E2 versus HD conditions. **(K)** Motifs enriched in the chromatin accessible sites in **[J]**.

Figure 5. NFKB pathway activation via RelA phosphorylation and binding is enhanced in hormone deprived conditions (A) Immunoblot of whole cell lysates for the NFKB subunits, RelA and RelB, and ER in MCF7 cells grown with estradiol (E2) 10 nM or in hormone deprived (HD) conditions

in response to IFNg 10 ng/mL stimulation. **(B)** Whole cell lysate immunoblots of ER, RelA and phospho-RelA (Ser536) in MCF7 cells. Hormone deprived cells were stimulated with estradiol (10 nM) for 4 days. Protein was extracted every 24 hours. GAPDH was used as loading control. **(C)** Tornado plots of RelA binding sites in HD cells or treated with 10 nM estradiol with or without IFNg stimulation (10 ng/mL for 1h). **(D)** Volcano plot showing differential expression from RNA-seq of MCF7 cells in HD deprived conditions versus E2 treated conditions. Blue dots (True) denote genes that are differentially expressed based on RNA-seq and predicted to be regulated by RelA based on RelA ChIP-seq and BETA minus analysis. The orange dots (False) represent the genes that are differentially expressed between HD and E2 conditions but not predicted to be regulated by RelA based on the RelA ChIP-seq data. The p-value represents the significance of the association between RelA ChIP-seq and RNA-seq up HD (p-value=1.9 E-11) or down in HD (p-value = 0.156) compared to E2 stimulated cells without IFNg based on BETA basic. **(E)** GSVA of the HD_RelA gene set (541 genes) in primary ER+ breast cancers pre and post-neoadjuvant treatment with an AI. **(F-G)** RNAseq differential expression after RelA knockout (KO) compared to control. Volcano plot highlighting genes differently expressed between RelA KOs and RelA wt cells grown in HD conditions **[F]**, treated with fulvestrant (10 nM) **[G]** or grown in E2 conditions **(H)** for 72h and stimulated with IFNg (10 ng/mL) for the last 6 hours (h). n is the number of genes differentially expressed. **(I)** RelA ChIP-seq tracks showing examples of RelA peaks at the promoter region of IFNg associated genes in MCF7 cells grown in the presence of estradiol (E2) or in hormone deprived (HD) conditions and stimulated +/- IFNg (10 ng/mL) for one hour. **(J)** mRNA expression levels of ICAM1, HLA-A, TAP1, B2M and CXCL10 in E2 and HD conditions without and with RELA silencing (KO=knockout) after 6 hours of IFNg stimulation (*p-value<0.05; **p-value<0.01; ***p-value< 0.001. Error bars are mean ± s.d of at least 2 replicates per each KO. Two-way ANOVA).

Figure 6. Birinapant potentiates the antitumoral effect of ER blockade.

(A) Cell growth studies of MCF7 cells treated with vehicle (DMSO), fulvestrant, birinapant and the combination of fulvestrant and birinapant for 7 days. Number of cells were measured at day 0, 3, 5 and 7. (*p-value<0.05, error bars represent S.D. from four replicates, two-way ANOVA). **(B)** Synergy study of the combination of fulvestrant and birinapant MCF7 cells. Synergy was calculated based on the ZIP reference model using SynergyFinder (www.synergyfinder.org). Deviations between observed and expected responses with positive and negative values denote synergy and antagonism respectively. **(C)** ER+ /HER2- PDX tumor growth study (**p-value<0.01; ***p-value< 0.001, error bars represent S.D (N=5 mice per group), two-way ANOVA). **(D)** Gene set enrichment analysis (GSEA) of genes differentially expressed in MCF7 cells after treatment with fulvestrant (10 nM), birinapant (100 nM) or the combination compared to vehicle (DMSO) control. The size of each circle indicates the q-value (genes sets with a q-value of <0.25 in at least one condition were included), the color scale indicates the normalized enrichment score (NES).

Figure 7. Birinapant and fulvestrant enhance antigen presentation, T-cell migration and T-cell mediated cytotoxicity. (A) mRNA expression levels of IFNg and antigen presentation related genes in MCF7 cells that were treated with vehicle control (DMSO), fulvestrant (10 nM), birinapant (100 nM) and the combination of fulvestrant and birinapant for 3 days and stimulated with IFNg for the last 24 hours. **(B-E)** MFI quantification of MHC-I and PD-L1 levels assessed by flow cytometry in MCF-7 cells grown in hormone deprived (HD) or in the presence of estradiol (E2) **(B,C)** or treated with fulvestrant (10 nM) **(D,E)**, and treated with the addition of with doses of birinapant for 3 days. Cells were stimulated with IFNg (10 ng/mL) for the last 24 hours. MFI levels are relative to no-IFNg conditions (*p<0.05; ***p< 0.001; n.s., not significant). Error bars are mean ± s.d of at least 2 replicates. **(F)** Whole cell lysates immunoblots of ER, NFKB subunits and IFNg target genes in MCF7

cells grown treated with vehicle control (DMSO), fulvestrant (10 nM), birinapant (100 nM) and the combination with and without IFNg (10 ng/mL) stimulation for 24 hours. **(G)** Representative immunofluorescence images from T cell migration assay after treatment with vehicle control (DMSO), fulvestrant (10 nM), birinapant (100 nM) and the combination MCF-7 cells were pretreated and seeded in the AIM 3D Cell Culture Chips. Primary CD8+ T-cells stained with CellTrace Red Stain were seeded on the lateral channels **(H)** Quantification of migration to the matrix was measured after 5 days (*$p<0.05$. Error bars are mean ± s.d of at least 5 replicates. Two-way ANOVA). **(I)** Representative figures of immunofluorescent stains of co-cultured MCF7_NYESO1 and T- cells transduced with NYESO1 specific TCR. Immunofluorescent stains include MHC-I (red) Granzyme B (green), Actin (yellow), DAPI for nuclear staining (blue) and a merge image. **(J)** MCF7 cells expressing specific NYESO1 antigen were pretreated with vehicle (DMSO), fulvestrant (10 nM), birinapant (100 nM) and the combination of both drugs and cocultured with primary NYESO1 TCR+ T cells for 16 hours. Number of cancer cells alive were measured and data is relative to MCF7_NYESO1 grown without T cells (*$p<0.05$; ***$p<0.001$; n.s., not significant. Error bars are mean ± s.d of at least 3 replicates. Two-way ANOVA).

Figure 1

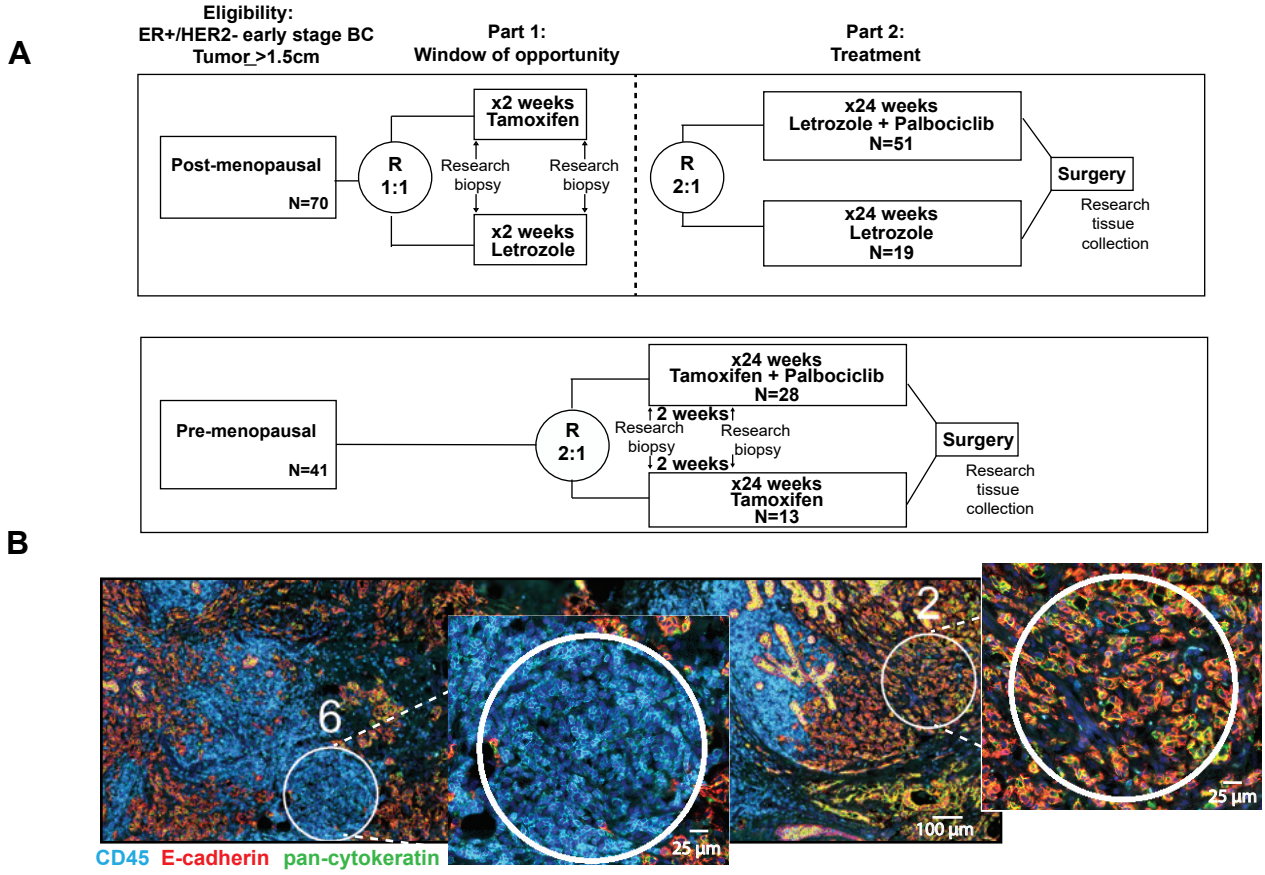

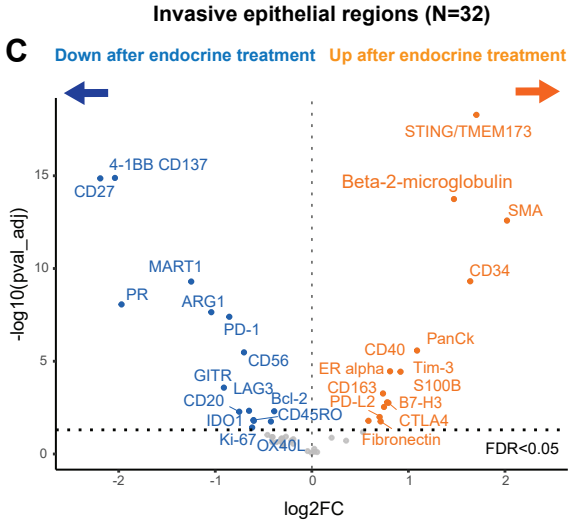

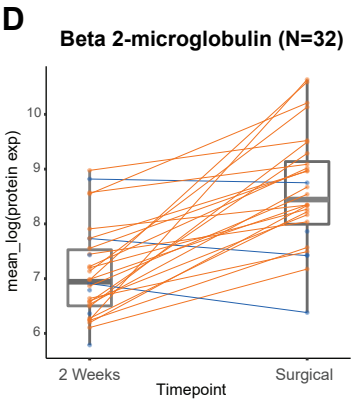

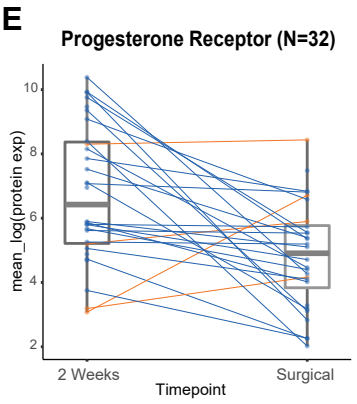

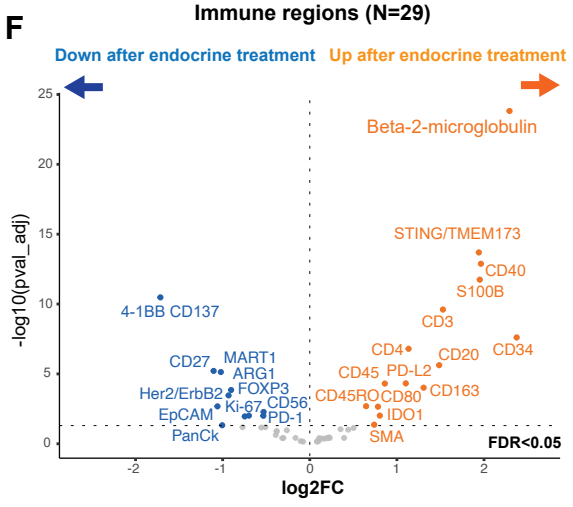

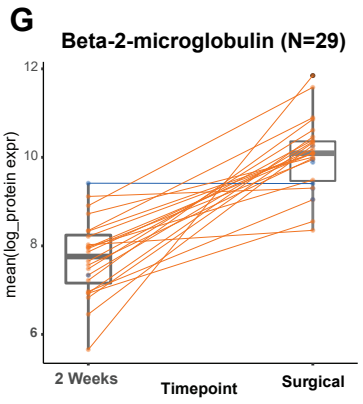

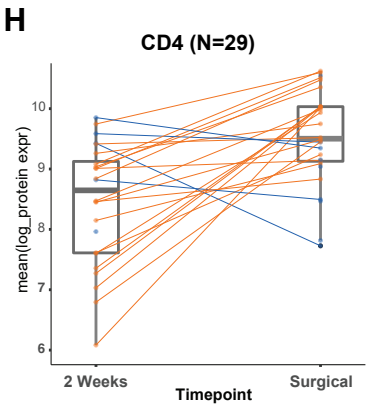

Figure 2

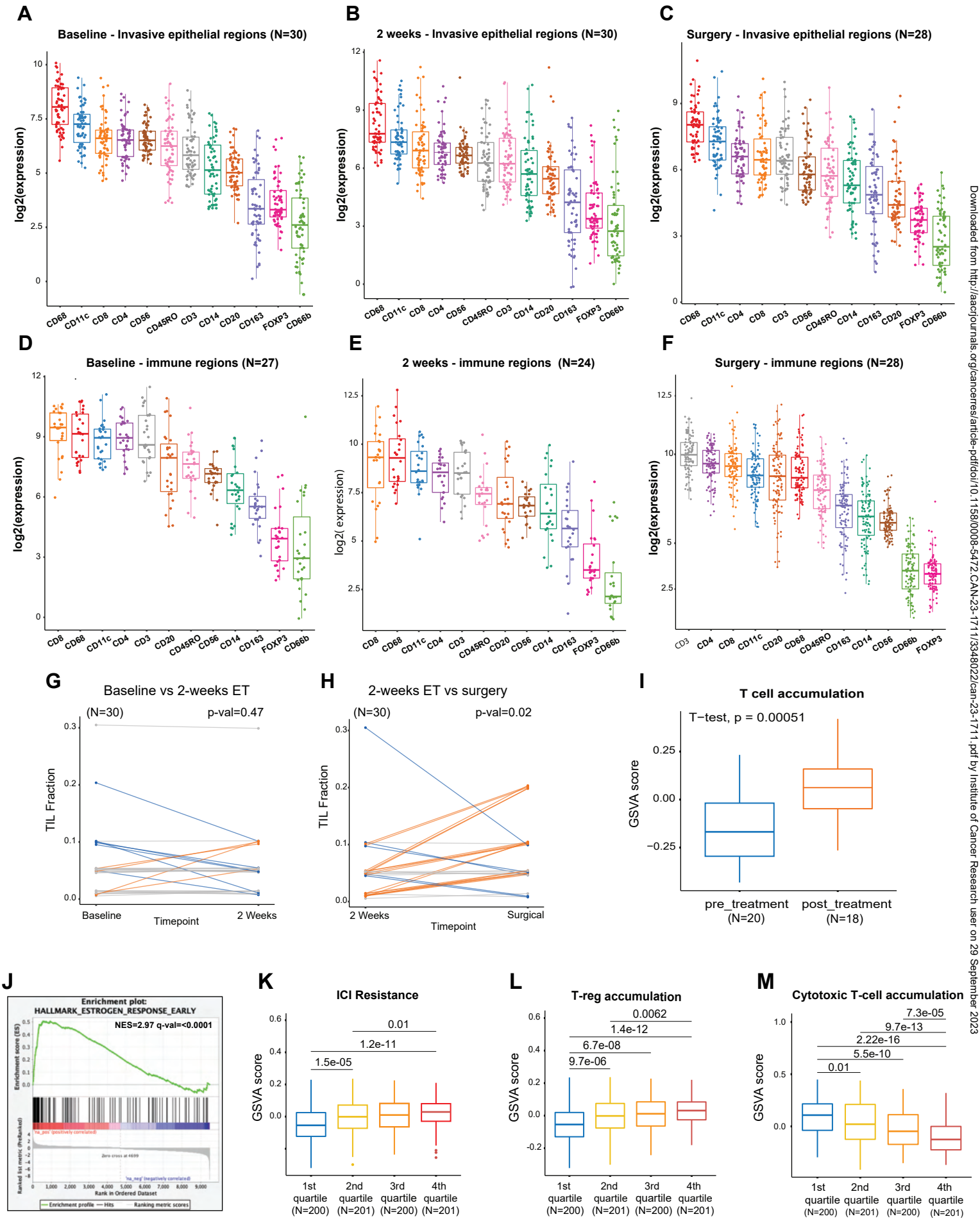

Figure 3

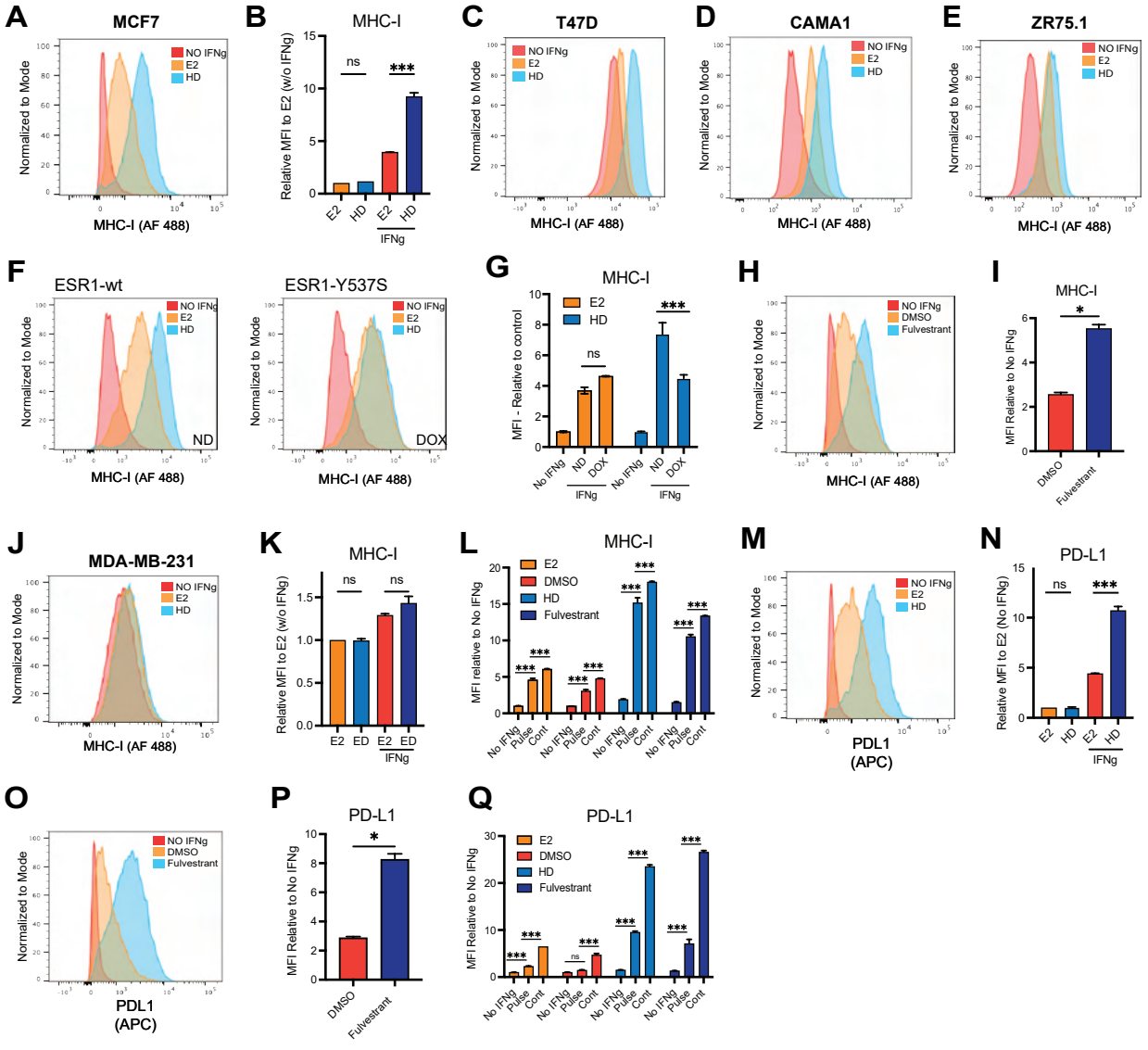

Figure 4

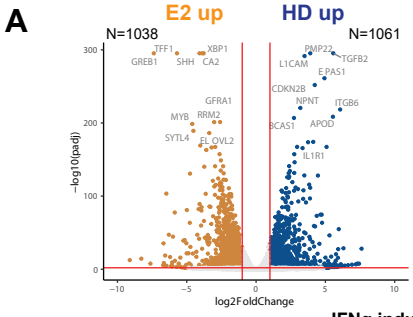

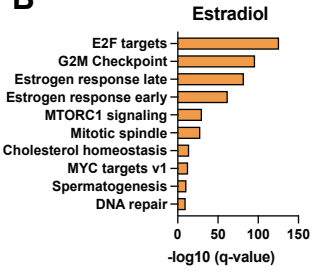

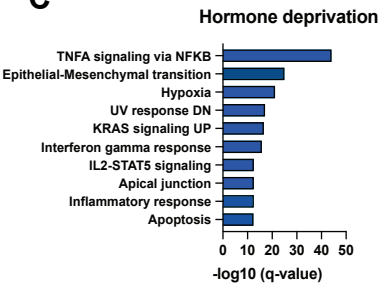

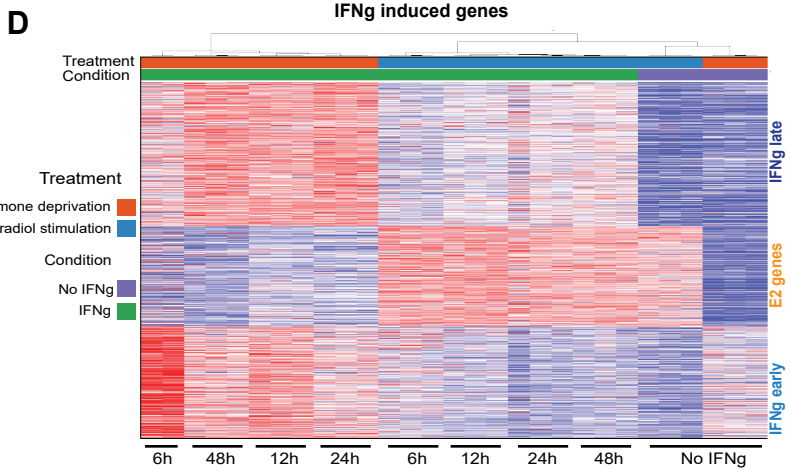

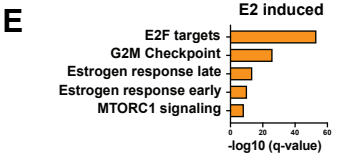

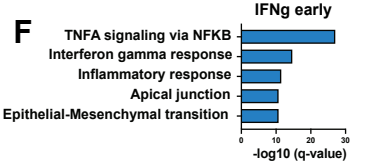

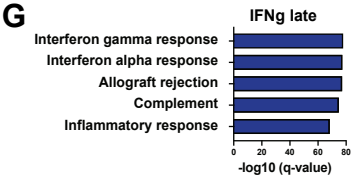

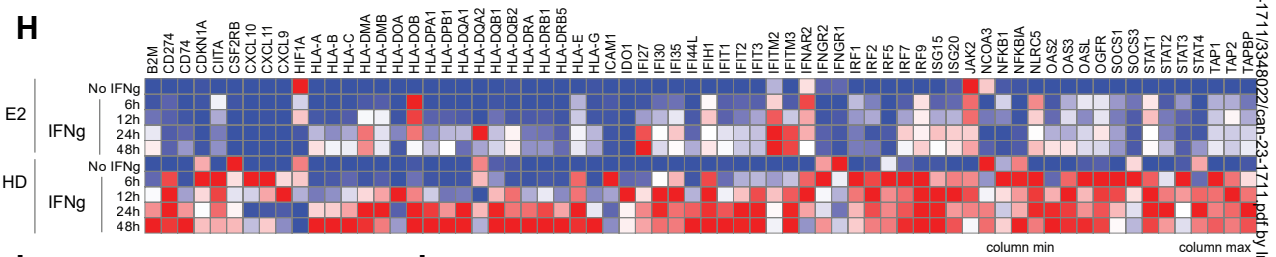

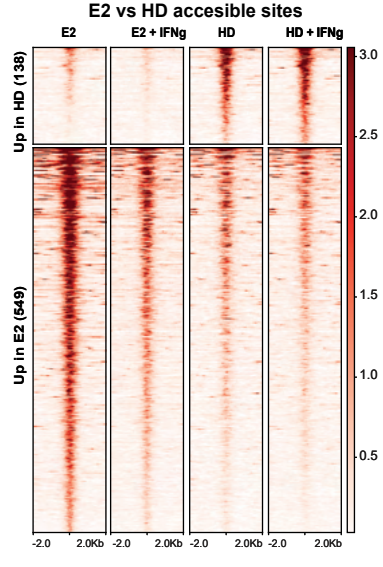

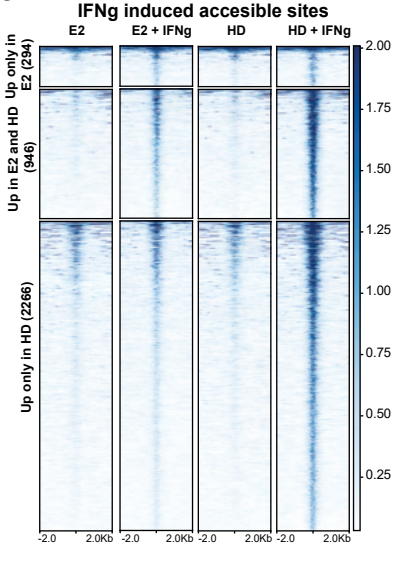

K

Motif		E2 p-value	E2 and HD p-value	HD p-value
	IRF2	1E-100	1E-563	1E-1583
	ISRE/IRF3	1E-92	1E-466	1E-1200
	IRF1	1E-91	1E-540	1E-1526
	RELA	-	-	1-E2

Figure 5

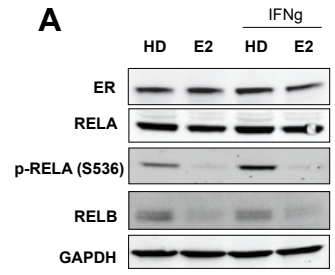

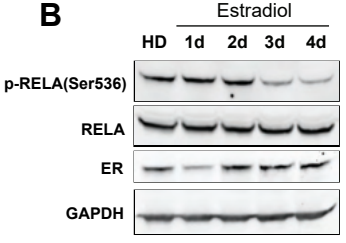

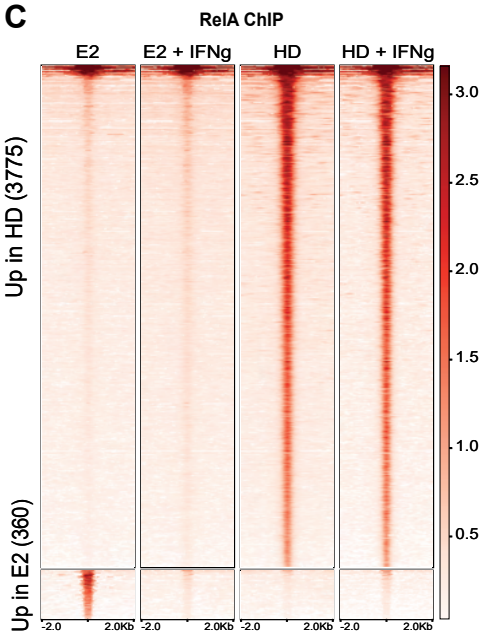

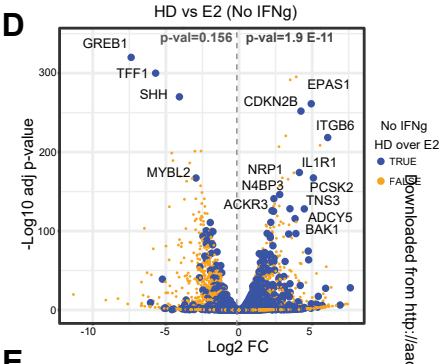

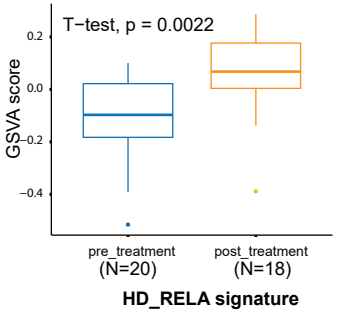

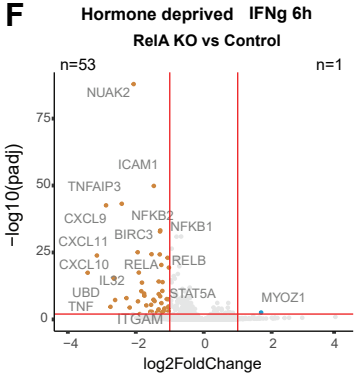

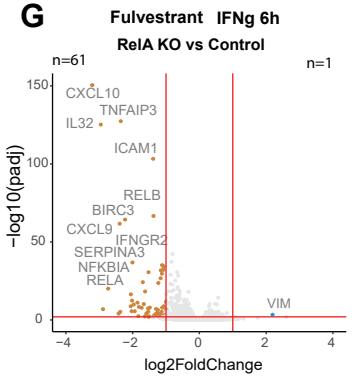

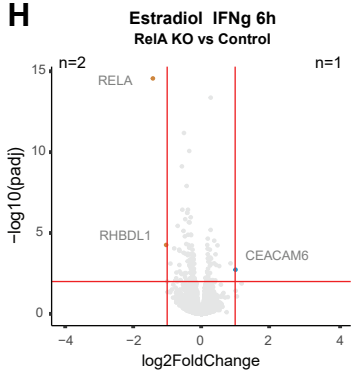

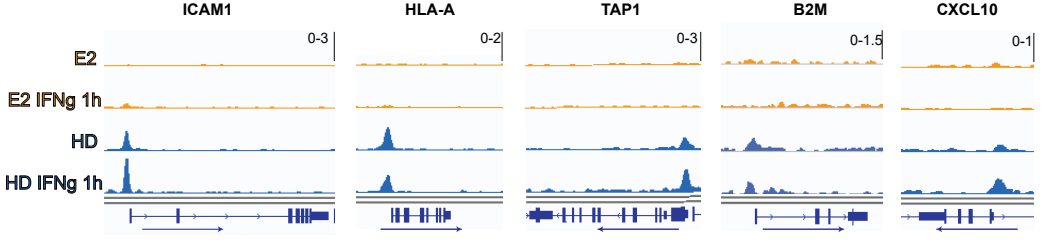

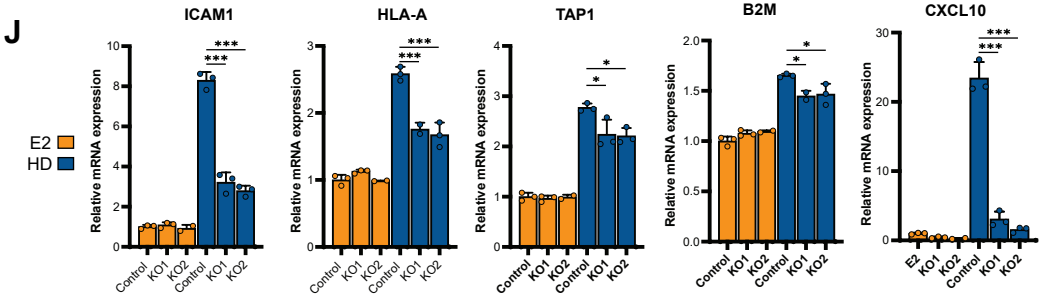

Figure 6

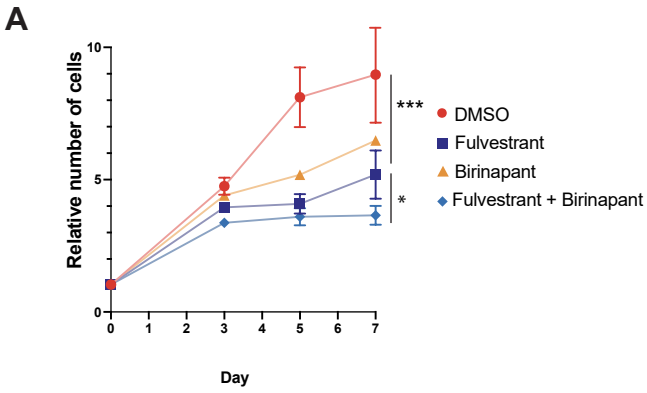

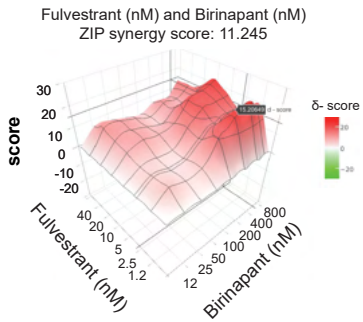

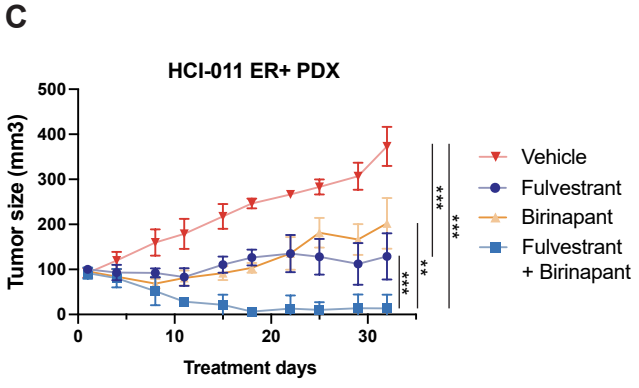

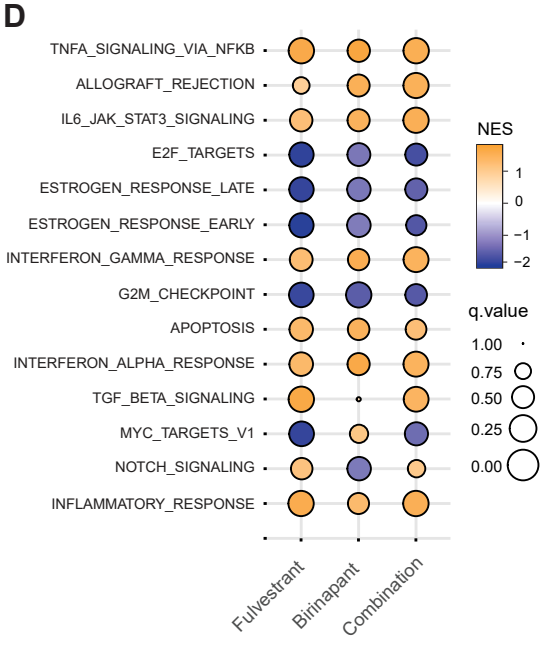

Figure 7